Light diffraction from opal-based photonic crystals with growth-induced disorder: Experiment and theory

A. V. Baryshev, V. A. Kosobukin, K. B. Samusev, D. E. Usvyat, and M. F. Limonov
Ioffe Physico-Technical Institute, Politekhnicheskaya 26, 194021 St. Petersburg, Russia
(Received 28 July 2005; revised manuscript received 19 January 2006; published 23 May 2006)

We report on a comprehensive experimental and theoretical study of light diffraction from synthetic opals. A general theory of coherent elastic scattering (Bragg diffraction) is proposed, taking into account growth-induced effects of interlayer disorder and the refraction of light waves due to a background dielectric permittivity. The diffraction patterns were investigated using monochromatic or white light illumination in various scattering geometries. It is shown that the scattering of a monochromatic beam produces a set of diffraction spots (reflexes), which obey the conditions for Bragg light reflection by the {*hkl*} crystal planes in a twinned face-centered cubic (fcc) structure made up of closely packed amorphous silica spherical particles. The white light diffraction patterns registered in different geometries are analyzed for a one dimensional (1D) disorder in hexagonal closely packed layers normal to the growth axis. The data analysis is performed in terms of the suggested diffraction theory of photonic crystals, taking into account the effects of random 1D packing of growing layers. A good quantitative agreement between the experimental data and calculations has been obtained for all diffraction patterns, including the angular and spectral dependencies of the radiation intensity. We have also estimated the statistical parameters of the opal structure composed of fcc lattice twins of random lengths along the sample growth axis. The long-wavelength diffraction edge is found for the principal scattering geometries.

DOI: 10.1103/PhysRevB.73.205118 PACS number(s): 42.70.Qs, 42.25.Fx, 42.79.Fm

I. INTRODUCTION

The phenomenon of Bragg diffraction of waves having various physical nature (x rays, neutrons, electrons) underlies many techniques used for the study of the atomic structure of crystals.[1] Bragg diffraction gives rise to energy (frequency) bandgaps in the spectrum for the wave propagation in a periodic structure.[2] The presence of bandgaps, termed stop bands, along certain directions of electromagnetic wave propagation or of a full bandgap along all directions is the major feature of a periodic dielectric structure known as a photonic crystal.[3] For a bandgap to arise, the period of the spatial modulation of dielectric permittivity should be comparable with the light wavelength.

Currently, there is much interest in the fabrication and study of photonic crystals possessing bandgaps in various spectral regions, from the microwave range[4] to the visible.[5] Materials with photonic energy gaps do not occur naturally, except for the well-known gemstone natural opal with brilliance light scattering in the visible. Both natural and synthetic opals consist of closely packed monodisperse spherical particles of amorphous silica (a-SiO_2), having a submicron size close to the visible light wavelength. The authors of Ref. 6 suggested the application of opals as three-dimensional (3D) photonic crystals for the visible spectral range. At present, many other types of photonic crystals for the visible are being studied, among them opal-based materials such as synthetic opals with different fillings[7–15] and inverted opals,[16–18] as well as structurally related materials with air spheres in titania (TiO_2)[19–21] and various colloidal crystals.[22–25] The optical properties of photonic crystals, mostly synthetic opals and related structures, were studied in many works using spectroscopic techniques. Additionally, there has been much activity on the measurement of specular reflection spectra from the (111) plane in materials with air spheres in titania[20,21] and from various colloidal crystals.[24,25]

The Bragg diffraction as a key optical phenomenon in photonic crystals has not been intensively examined, either experimentally or theoretically, for opals or opal-based materials. The 3D Bragg diffraction in synthetic opals was investigated in Ref. 26, but this work primarily dealt with the visualization of the photonic bandgap structure through the diffraction patterns. An especially important conclusion from this study is that the diffraction patterns can serve as a visual indicator of stop bands along certain crystallographic directions and allow the identification of diffraction processes responsible for the formation of observable bandgaps in perfect and weakly disordered photonic structures. The results of Ref. 26 have also demonstrated that the Bragg spots (reflexes) registered in visible range provide direct information on the opal crystal structure. The earlier report on this effect in natural opals[27] was largely descriptive, the sample orientation was not identified, and the diffraction was not analyzed theoretically. A recent paper[28] reports on the Bragg diffraction of light in colloidal crystals made up of polystyrene spheres. Also, another recent paper[29] presents some diffraction patterns measured for the only [111] growth direction of opals. However, the general properties of the 3D Bragg diffraction in synthetic opals and related materials still remain unclear.

The recent effort to analyze photonic crystals using Bragg light diffraction[26] is, in some respects, similar to an x-ray diffraction study of atomic crystals.[30] So, from the very beginning, it is worth emphasizing the similarities and differences in the Bragg diffraction of light waves from photonic crystals and of x rays from atomic crystals. The similarity

between the two types of electromagnetic diffraction, as well as the diffraction of waves of any physical nature by media with periodically modulated response functions, is associated with the coherence of this kind of elastic scattering. This brings us to the structure factor and the Laue equations stating that the principal change in the wave vector in such media is equal to an integer of the reciprocal lattice vector. However, the issue of special interest to us is the essential differences between the two types of electromagnetic diffraction. These originate from the distinctions in (1) the dielectric response functions, (2) the lattice period, (3) the particle size and shape (the a-SiO_2 spheres in the case of opals), and (4) the wavelength range under study. To compare, the periodic variation in the dielectric constant for x rays that is responsible for the stop bands is $\sim 10^{-5}$; so the stop bands are extremely narrow,[30] whereas the occurrence of a full bandgap is impossible. For this reason, the x-ray experiments usually deal with angle-resolved (directional) measurements of diffraction patterns.[30] What is essential in photonic crystals is the presence of wide enough energy stop bands in the wavelength range from ultraviolet, to infrared, where the contrast in the dielectric constants becomes large enough for a full photonic bandgap to appear. It is natural to study them by spectroscopic methods, mostly using the reflection and transmission spectra in the bandgap region. Besides, an essential increase in the dielectric permittivity for visible light has important consequences that have no analogs for x rays. First, light refraction may arise at the crystal surface and, second, diffracted waves propagate in a medium characterized by a nonvacuum dielectric background. Finally, the constituting particle size and the lattice constant of a photonic crystal can be technologically varied such that the principal diffraction occurs in the visible, while the higher-order diffraction spots are invisible to the human eye.

Our aim in the present work was to study experimentally the Bragg diffraction from synthetic opal crystals of various quality, from perfect to strongly disordered ones, and to develop a diffraction theory for real opal-like photonic crystals. The diffraction patterns were investigated in various scattering geometries, keeping in mind that the diffraction may be considerably complicated by the sample growth disorder. The diffraction patterns obtained did show the presence of a twinned face-centered cubic (fcc) structure with a 1D disorder in the alternating hexagonal closely packed (hcp) layers normal to the growth axis. Our theory of light diffraction from a twinned opal structure is capable to take into account the major features observed experimentally. These are the presence of a long-wavelength diffraction edge varying with the crystal orientation, the spectral and angular characteristics of the diffracted beam intensity, and the relationship between the observed diffraction patterns and a twinned fcc structure. Besides, we have found some statistical characteristics of the twinned sample structure, in particular, the fcc packing probability, which indicates that the cubic lattice is largely composed of the fcc phase.

The paper is organized as follows. In Sec. II we present a general theory of Bragg diffraction in photonic crystals, bearing in mind the effects of the background dielectric constant and growth-induced interlayer disorder, which are discussed with reference to opal-like structures. In Sec. III we describe the structure of synthetic opals and the samples under study, while in Sec. IV we outline the experimental setup and the scattering geometries. In Sec. V we discuss the experimental results on the Bragg diffraction in opals. The data are analyzed and interpreted in the framework of the developed theory of Bragg diffraction in disorder-affected opal structures.

II. THEORETICAL BACKGROUND

At first glance, the Bragg diffraction of visible light and that of x rays look alike, so we will focus here on their principal differences that constitute the specificity of photonic crystals as diffraction objects. In this section, we develop a consistent theory to consider the essential structural and dielectric aspects of Bragg diffraction in photonic crystals that seem to have not been properly treated in the literature. The theory takes into account the inherent interlayer disorder that occurs due to a specific growth mechanism in a variety of self-organized photonic crystals. This kind of structural randomness has been observed in such photonic crystals as opals,[12,14,15,31] inverted opals,[32] colloidal structures,[23] and some other materials.

We treat Bragg diffraction as coherent elastic scattering of light by perfect or disorder-affected photonic crystals, whose dielectric permittivity is spatially modulated with a period comparable with the light wavelength. We will show, in particular, that the theory can interpret the reflection due to the crystal surface (the background dielectric constant), whose effect can interfere with the Bragg diffraction from a real photonic crystal. Next, we consider the kinematics of the Bragg diffraction from a perfect reference fcc lattice to apply the results to the analysis of diffraction by slightly disordered photonic crystals. Finally, a statistical consideration of the diffraction intensity is presented for 3D closely packed opal-like structures made up of random sequences of three possible positions of 2D hcp layers. The predictions and conclusions from the theoretical treatment are applied in Sec. V to interpret our experimental data on synthetic opals.

A. Basic equations

We can describe the spatially modulated dielectric permittivity of a photonic crystal as

$$\epsilon(\mathbf{r}) = \epsilon_0 + \delta\epsilon(\mathbf{r}). \tag{1}$$

By averaging over the crystal volume V, the uniform background dielectric constant

$$\epsilon_0 = \frac{1}{V}\int_V d\mathbf{r}\cdot\epsilon(\mathbf{r}) \tag{2}$$

is introduced in Eq. (1). The permittivity variation $\delta\epsilon(\mathbf{r}) = \delta\epsilon(\mathbf{r}+\mathbf{a}_i)$, periodic with the unit translations $\mathbf{a}_i$ of the crystal lattice is responsible for the Bragg diffraction, whose kinematics is defined by the orientation of the crystal planes specified by the reciprocal lattice, vector $\mathbf{b}$. For a perfect crystal, the modulation term in Eq. (1) is expanded into the Fourier series

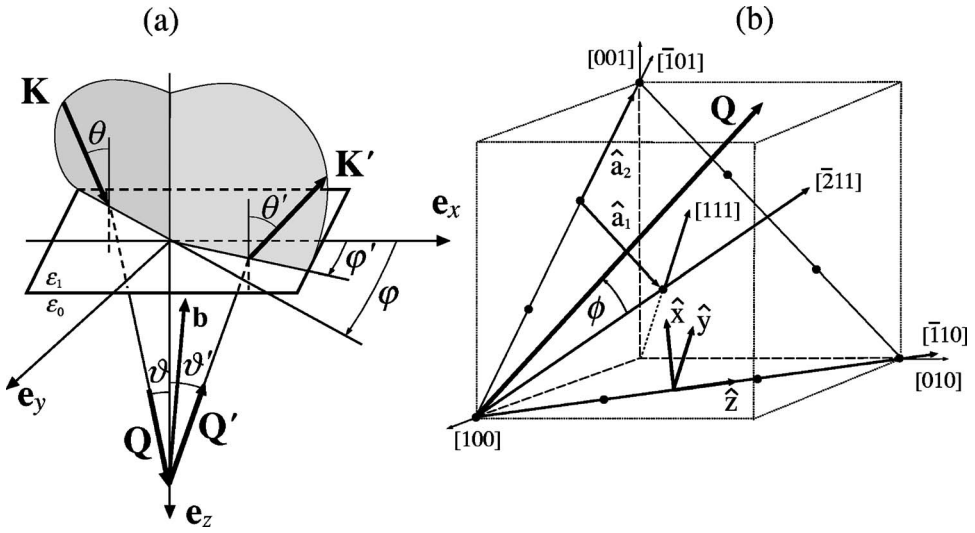

FIG. 1. (a) Optical scheme showing the relation between the vectors $\mathbf{K}$ of the incident wave and $\mathbf{K}'$ of the diffracted wave (measured outside the crystal) with the vectors $\mathbf{Q}$ and $\mathbf{Q}'$ entering the in-crystal diffraction condition $\mathbf{Q}'=\mathbf{Q}+\mathbf{b}$, where $\mathbf{b}$ is the reciprocal lattice vector. (b) The principal crystallographic directions in the reference fcc lattice and the in-crystal unit vectors $\hat{\mathbf{x}}\|[\bar{1}\bar{1}2]$, $\hat{\mathbf{y}}\|[111]$, and $\hat{\mathbf{z}}\|[\bar{1}10]$ used in the Bragg diffraction analysis. The unit translations $\hat{\mathbf{a}}_1$ and $\hat{\mathbf{a}}_2$ from Eq. (A1) are shown for a hcp layer.

$$\delta\epsilon(\mathbf{r})=\sum_{\mathbf{b}(\neq 0)}\delta\epsilon_{\mathbf{b}}\,e^{i\mathbf{b}\cdot\mathbf{r}},\quad \delta\epsilon_{\mathbf{b}}=\frac{1}{v_0}\int_{\mathbf{v}_0}d\mathbf{r}\cdot e^{-i\mathbf{b}\cdot\mathbf{r}}\delta\epsilon(\mathbf{r})=\delta\epsilon^{*}_{-\mathbf{b}}, \tag{3}$$

where v_0 is the unit cell volume. Disordering of the crystal violates the long-range order expressed by Eq. (3), but the diffraction features due to the short-range order survive, which is typical of the atomic structure of noncrystalline solids.[33]

In what follows, we assume that a photonic crystal occupies the half-space $z>0$, in which region the dielectric function obeys Eq. (1) with the background contribution (2). The zeroth-order approximation ($\delta\epsilon=0$) takes into account only the background permittivity $\epsilon^0(z)$ equal to ϵ_1, if $z<0$, and to ϵ_0, if $z>0$, as seen in Fig. 1(a). The plane $z=0$, where the dielectric function $\epsilon^0(z)$ jumps from ϵ_1 to ϵ_0, represents the optical boundary of a photonic crystal specularly reflecting the incident waves, irrespective of the orientation of the crystallographic planes. In general, the monochromatic (with the frequency ω) zeroth-order electric field $\mathbf{E}^0$ and the related tensorial Green function $\hat{G}^0$, and the total field $\mathbf{E}$ can be found from the equations

$$[\mathrm{curl}\,\mathrm{curl}-\epsilon^0(z)k_0^2]\begin{pmatrix}\mathbf{E}^0(\mathbf{r})\\ \hat{G}^0(\mathbf{r},\mathbf{r}')\\ \mathbf{E}(\mathbf{r})\end{pmatrix}=\begin{pmatrix}0\\ \delta(\mathbf{r}-\mathbf{r}')\hat{I}\\ \delta\epsilon(\mathbf{r})k_0^2\mathbf{E}(\mathbf{r})\end{pmatrix}. \tag{4}$$

Here, $k_0=\omega/c$, c is the velocity of light in vacuum, $\hat{I}$ is the unit matrix with the elements $I_{\alpha\beta}=\delta_{\alpha\beta}$, α and β are the Cartesian indices, and $\delta_{\alpha\beta}$ is the Kroneker delta.

In the presence of the perturbation $\delta\epsilon(\mathbf{r})$, the solution of the third of Eqs. (4) for the field outside the crystal ($z<0$) is

$$E_\alpha(\mathbf{r})=E^0_\alpha(\mathbf{r})+k_0^2\sum_\beta\int d\mathbf{r}'\,G^0_{\alpha\beta}(\mathbf{r},\mathbf{r}')\delta\epsilon(\mathbf{r}')\tilde{E}_\beta(\mathbf{r}'), \tag{5}$$

Hereafter, the overtilde will indicate the fields inside the crystal ($z>0$) satisfying the self-consistent integral equation

$$\tilde{E}_\beta(\mathbf{r})=\tilde{E}^0_\beta(\mathbf{r})+k_0^2\sum_\gamma\int d\mathbf{r}'\,\tilde{G}^0_{\beta\gamma}(\mathbf{r},\mathbf{r}')\delta\epsilon(\mathbf{r}')\tilde{E}_\gamma(\mathbf{r}'). \tag{6}$$

To solve Eqs. (4)–(6), we will assume that a wave with the linear polarization τ, the amplitude E^{inc}_τ, and the wave vector

$$\mathbf{K}=\boldsymbol{\kappa}+\mathbf{e}_z k_1,\quad \boldsymbol{\kappa}=\sqrt{\epsilon_1}k_0\sin\theta(\mathbf{e}_x\cos\varphi+\mathbf{e}_y\sin\varphi),$$
$$k_1=\sqrt{\epsilon_1}k_0\cos\theta \tag{7}$$

is incident onto the crystal from the half-space $z<0$. Equations (7) are expressed in the Cartesian coordinates with the unit vectors $\mathbf{e}_\alpha$, in which the beam direction can be given by the spherical polar θ and azimuth φ angles, as indicated in Fig. 1(a). At $z<0$, the first of Eqs. (4) yields

$$E^0_\alpha(\mathbf{r})=E^{\mathrm{inc}}_\tau e^\tau_\alpha(\mathbf{K})\exp(i\boldsymbol{\kappa}\cdot\boldsymbol{\rho})[\exp(ik_1z)+r^0_\tau(\kappa)\exp(-ik_1z)], \tag{8}$$

for the tangential field components ($\alpha=x,y$) and $E^0_z(\mathbf{r})=(i/k_1^2)d[\boldsymbol{\kappa}\cdot\mathbf{E}^0(\mathbf{r})]/dz$ for the normal component with $\mathbf{r}=(\boldsymbol{\rho},z)$ and $\boldsymbol{\rho}=(x,y)$. In Eq. (8), the polarization unit vectors $\mathbf{e}^\tau$ are

$$\mathbf{e}^p(\mathbf{K})=(\mathbf{e}_x\cos\varphi+\mathbf{e}_y\sin\varphi)\cos\theta-\mathbf{e}_z\sin\theta,$$
$$\mathbf{e}^s(\mathbf{K})=-\mathbf{e}_x\sin\varphi+\mathbf{e}_y\cos\varphi, \tag{9}$$

for p- and s-polarized waves, respectively. The Fresnel coefficients r^0_τ for the reflection from the background surface $z=0$ are

$$r^0_p=\frac{\epsilon_1 k-\epsilon_0 k_1}{\epsilon_1 k+\epsilon_0 k_1},\quad r^0_s=\frac{k_1-k}{k_1+k}, \tag{10}$$

where $k(\kappa)=\sqrt{\epsilon_0 k_0^2-\kappa^2}$. Inside the crystal ($z>0$), the tangential components of the unperturbed field entering Eq. (6) have the form

$$\tilde{E}^0_\alpha(\mathbf{r})=E^{\mathrm{inc}}_\tau t^0_\tau(\kappa)e^\tau_\alpha(\mathbf{Q})\exp(i\mathbf{Q}\cdot\mathbf{r}), \tag{11}$$

with $t^0_\tau=1+r^0_\tau$. In accordance with Fig. 2, the in-crystal wave vector

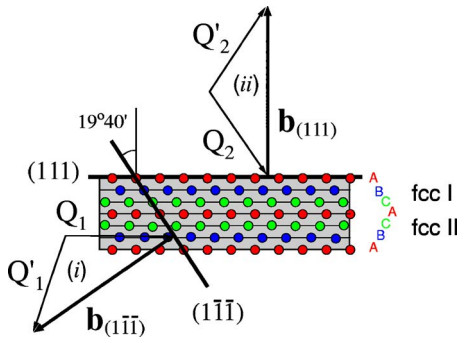

FIG. 2. (Color online) Scheme of the Bragg diffraction in opals. The diffraction kinematic triangles for the incidence geometries denoted as (*i*) and (*ii*) in text (the vectors $\mathbf{b}_{(1\bar{1}\bar{1})}$ and $\mathbf{b}_{(111)}$ are shown as an example). The triangle (*i*) presents the diffraction $\mathbf{Q}_1 \rightarrow \mathbf{Q}_1'$ with $\mathbf{Q}_1 \| (111)$ and the triangle (*ii*) presents the diffraction $\mathbf{Q}_2 \rightarrow \mathbf{Q}_2'$ from the (111) planes. The adjacent domains of the fcc-I and fcc-II lattices are shown to form a twin. The nonequivalence of the (111) and $(1\bar{1}\bar{1})$ planes in the twinned fcc structure is clearly seen.

$$\mathbf{Q} = \boldsymbol{\kappa} + \mathbf{e}_z k, \quad k = \sqrt{\epsilon_0} k_0 \cos\vartheta, \tag{12}$$

is related to the out-crystal vector $\mathbf{K}$ in Eq. (7) by the Snell law $\sqrt{\epsilon_1}\sin\theta = \sqrt{\epsilon_0}\sin\vartheta = \kappa/k_0$ (continuity of the wave vector $\boldsymbol{\kappa}$) for the light at the boundary $z=0$. The unit vectors $\mathbf{e}^{\tau}(\mathbf{Q})$ are derived from Eq. (9) by substituting $\theta \rightarrow \vartheta$. The in-crystal $\mathbf{Q}'$ and out-crystal $\mathbf{K}'$ wave vectors of the scattered light are then found by the substitutions $\varphi \rightarrow \varphi'$, $\vartheta \rightarrow \pi - \vartheta'$ and $\theta \rightarrow \pi - \theta'$ in expressions of the form (7)–(9) for $\mathbf{K}$ and (12) for $\mathbf{Q}$. The angles ϑ' and θ' are taken from the negative direction of $\mathbf{e}_z$, in accordance with Fig. 1(a). Because of the elastic scattering, we further imply the equalities $|\mathbf{Q}'| = |\mathbf{Q}| = \sqrt{\epsilon_0} k_0$ and $|\mathbf{K}'| = |\mathbf{K}| = \sqrt{\epsilon_1} k_0$.

B. Observable quantities

The Born approximation of the scattering theory is usually sufficient to interpret the diffraction of waves from atomic crystals and disordered solids.[33] Similarly, keeping in mind that opal-based photonic crystals have a low dielectric contrast ($|\delta\epsilon_{\mathbf{b}}| \ll \epsilon_0$), we calculate the diffraction intensity in the Born approximation, assuming $\tilde{\mathbf{E}} \approx \tilde{\mathbf{E}}^0(\mathbf{r}) \equiv \tilde{\mathbf{E}}^0(\mathbf{Q})\exp(i\mathbf{Q}\cdot\mathbf{r})$ in the integrand of Eq. (6). Therefore, the field $\tilde{\mathbf{E}}$ will have the same linear polarization τ as the unperturbed field $\tilde{\mathbf{E}}^0$, and the radiation field $\mathbf{E}' = \mathbf{E} - \mathbf{E}^0$ outside the crystal due to the perturbation $\delta\epsilon(\mathbf{r})$ can be calculated from Eq. (5) under the conditions (8) and (11). In the lowest-order approximation in $\delta\epsilon$, the asymptotic expression for the field radiated from the crystal into the back hemisphere ($z<0$, $\sqrt{\epsilon_1} k_0 r \gg 1$, $r = \sqrt{\rho^2 + z^2}$) is evaluated by the steepest descent technique:[34,35]

$$E'_{\alpha}(\mathbf{r}) = -\frac{i\sqrt{\epsilon_1} k_0^3 \cos\theta'}{2\pi} \frac{e^{i\sqrt{\epsilon_1} k_0 r}}{r} \sum_{\beta} D^0_{\alpha\beta}(0^-, 0^+; \boldsymbol{\kappa}') \times \left(\int_V \delta\epsilon(\mathbf{r}') e^{-i\mathbf{q}\cdot\mathbf{r}'} \, d\mathbf{r}' \right) \tilde{E}^0_{\beta}(\mathbf{Q}). \tag{13}$$

Here, the tensor $\hat{D}^0(z, z'; \boldsymbol{\kappa})$ is the $(z, \boldsymbol{\kappa})$ representation of the Green's function $\hat{G}^0(\mathbf{r}, \mathbf{r}') = \hat{G}^0(z, z'; \boldsymbol{\rho} - \boldsymbol{\rho}')$, and

$$\mathbf{q} = \mathbf{Q}' - \mathbf{Q} \tag{14}$$

is the scattering vector in the crystal. The direction of the vector $\mathbf{K}'$ of the outgoing wave (the spherical angles θ' and φ') is defined by the vector $\mathbf{r} = r[(\mathbf{e}_x \cos\varphi' + \mathbf{e}_y \sin\varphi')\sin\theta' - \mathbf{e}_z \cos\theta']$ of the observation point outside the crystal.

Next, we calculate the ratio of the Poynting vectors $S'_{\tau'} = (8\pi)^{-1} c\sqrt{\epsilon_1} |\mathbf{E}'_{\tau'}|^2$ of the τ'-polarized diffracted wave (13) outside the crystal ($z \rightarrow -\infty$) to $S^{\mathrm{inc}}_{\tau} = (8\pi)^{-1} c\sqrt{\epsilon_1} |\mathbf{E}^{\mathrm{inc}}_{\tau}|^2$ of the τ-polarized incident wave (8). This yields the following cross section for the scattering (diffraction) channel $\mathbf{K}, \tau \rightarrow \mathbf{K}', \tau'$ specified by the τ and τ' polarization indices:

$$\frac{d\sigma_{\tau\tau'}}{d\Omega'} = \frac{k_0^4}{16\pi^2} \left| \int_V \delta\epsilon(\mathbf{r}) e^{-i\mathbf{q}\cdot\mathbf{r}} \, d\mathbf{r} \right|^2 \cdot |t^0_{\tau}(\kappa)|^2 \times u_{\tau\tau'}(\boldsymbol{\kappa}, \boldsymbol{\kappa}') \cdot |t^0_{\tau'}(\kappa')|^2. \tag{15}$$

Here, $d\Omega' = \sin\theta' \, d\theta' \, d\varphi'$ is the solid angle in the back hemisphere, and $u_{pp} = \cos^2\theta'[\cos\vartheta\cos(\varphi' - \varphi) - \sin\vartheta \tan\vartheta']^2$, $u_{ps} = \cos^2\vartheta \sin^2(\varphi' - \varphi)$, $u_{sp} = \cos^2\theta' \sin^2(\varphi' - \varphi)$, $u_{ss} = \cos^2(\varphi' - \varphi)$. The cross section for nonpolarized light is

$$\frac{d\sigma}{d\Omega'} = \frac{1}{4} \sum_{\tau,\tau'} \frac{d\sigma_{\tau\tau'}}{d\Omega'}. \tag{16}$$

It follows from Eqs. (13) and (15) that the diffraction properties of a photonic crystal are mainly determined by the structure factor

$$S(\mathbf{q}) = \left| \frac{1}{\sqrt{N}} \sum_{\mathbf{n}} e^{i\mathbf{q}\cdot\mathbf{R}_{\mathbf{n}}} \right|^2 = \frac{1}{N} \sum_{\mathbf{n},\mathbf{n}'} e^{-i\mathbf{q}\cdot(\mathbf{R}_{\mathbf{n}'} - \mathbf{R}_{\mathbf{n}})}, \tag{17}$$

entering the term

$$\left| \int_V \delta\epsilon(\mathbf{r}) e^{-i\mathbf{q}\cdot\mathbf{r}} \, d\mathbf{r} \right|^2 = v_0 V |\delta\epsilon_{\mathbf{q}}|^2 S(\mathbf{q}). \tag{18}$$

Here, N is the number of unit cells having the volume v_0 within the crystal volume $V = v_0 N$. The form factor $|\delta\epsilon_{\mathbf{q}}|^2$ is expressed through the Fourier transform,

$$\delta\epsilon_{\mathbf{q}} = \frac{1}{v_0} \int_{v_0} \delta\tilde{\epsilon}(\mathbf{r} - \mathbf{R}_{\mathbf{n}}) e^{-i\mathbf{q}\cdot(\mathbf{r} - \mathbf{R}_{\mathbf{n}})} \, d\mathbf{r}, \tag{19}$$

of the function $\delta\tilde{\epsilon}(\mathbf{r} - \mathbf{R}_{\mathbf{n}})$, which is equal to $\delta\epsilon(\mathbf{r})$ within a Wigner-Seitz unit cell centered at the site $\mathbf{R}_{\mathbf{n}}$ and to zero outside the cell; so the dielectric function (1) is $\delta\epsilon(\mathbf{r}) = \Sigma_{\mathbf{n}} \delta\tilde{\epsilon}(\mathbf{r} - \mathbf{R}_{\mathbf{n}})$.

When analyzing the diffraction patterns, one should keep in mind that self-organized photonic crystals like opals grow as stacks of 2D hcp layers built up of identical dielectric spherical particles. Along the growth axis of a real 3D closely packed structure, the hcp layers may take accidentally one of the three positions A, B, or C, which are strictly ordered in a perfect fcc lattice.[1] In the presence of the interlayer disorder, the summation over the site indices $\mathbf{n} = (\mathbf{n}_{\|}, l)$ in Eq. (17) can be separated into intralayer (over $\mathbf{n}_{\|}$) and interlayer (over the layer numbers l) summations by us-

ing the representation $\mathbf{R}_{\mathbf{n}'-\mathbf{n}} \equiv \mathbf{R}_{\mathbf{n}'_{\parallel}-\mathbf{n}_{\parallel},0} + \mathbf{R}_{0,l'-l}$. After the averaging over the random vectors $\mathbf{R}_{0,l}$ (this operation is designated further as $\langle \ldots \rangle$), the structure factor (18) transforms to

$$\langle S(\mathbf{q}) \rangle = S_{\parallel}(\mathbf{q}) \langle S_{\perp}(\mathbf{q}) \rangle = S_{\parallel}(\mathbf{q}) \left\langle \frac{1}{L} \sum_{l,l'=1}^{L} e^{-i\mathbf{q}\cdot\mathbf{R}_{0,l'-l}} \right\rangle, \tag{20}$$

where L is the number of hcp layers in a stack. Here, $S_{\parallel}(\mathbf{q})$ stands for the structure factor of a single layer, appearing as a structural unit of both the fcc lattice and the random stack. The summation in Eq. (17) over the sites $\mathbf{n}_{\parallel}$ of the layer lattice defined by two in-layer unit translations $\hat{\mathbf{a}}_i$ yields

$$S_{\parallel}(\mathbf{q}) = \prod_{i=1,2} S_i(\mathbf{q}) = \prod_{i=1,2} \frac{1}{N_i} \frac{\sin^2(N_i \mathbf{q}\cdot\hat{\mathbf{a}}_i/2)}{\sin^2(\mathbf{q}\cdot\hat{\mathbf{a}}_i/2)}. \tag{21}$$

In the limit $N_i \to \infty$, each factor in Eq. (21) changes to the 2π-periodic delta function,

$$S_i(\mathbf{q}) = 2\pi \sum_{m_i} \delta(\mathbf{q}\cdot\hat{\mathbf{a}}_i - 2\pi m_i), \tag{22}$$

where m_i with $i=1,2$ are integers.

C. Diffraction by regular lattices

We will now analyze the kinematics of the Bragg diffraction from the reference fcc lattice and apply the results to opal-like crystals with a weak interlayer disorder. For a 3D lattice, the summation over l in Eqs. (17) or (20) with the interlayer unit translation $\hat{\mathbf{a}}_3$ gives

$$S_{\perp}(\mathbf{q}) = \frac{1}{L} \frac{\sin^2(L\mathbf{q}\cdot\hat{\mathbf{a}}_3/2)}{\sin^2(\mathbf{q}\cdot\hat{\mathbf{a}}_3/2)} \xrightarrow[L\to\infty]{} 2\pi \sum_{m_3} \delta(\mathbf{q}\cdot\hat{\mathbf{a}}_3 - 2\pi m_3), \tag{23}$$

where m_3 are integers. The maxima of the functions (22) and (23) correspond to the solutions of the Laue equations $\mathbf{q}\cdot\hat{\mathbf{a}}_i = 2\pi m_i$ with $i=1,2,3$ related to the perfect crystal lattice. Then, by expanding the scattering vector $\mathbf{q}$ in Eq. (14) in the basis vectors $\hat{\mathbf{b}}_i$ of the reciprocal lattice and taking account of $(\hat{\mathbf{a}}_i\cdot\hat{\mathbf{b}}_j) = 2\pi\delta_{ij}$, one can make sure that the equations $\mathbf{q}\cdot\hat{\mathbf{a}}_i = 2\pi m_i$ are indeed equivalent to the Bragg diffraction condition $\mathbf{q}=\mathbf{b}$, or

$$\mathbf{Q}' - \mathbf{Q} = \mathbf{b} \equiv \sum_i m_i \cdot \hat{\mathbf{b}}_i. \tag{24}$$

Using the dimensionless values

$$\zeta_{\alpha} = \frac{q_{\alpha}}{k_0\sqrt{\epsilon_0}}, \quad \boldsymbol{\beta} = \frac{a}{2\pi}\mathbf{b}, \tag{25}$$

Eq. (24) can be rewritten as

$$\boldsymbol{\zeta} = \Lambda\boldsymbol{\beta} = \Lambda \sum_i m_i \boldsymbol{\beta}_i, \tag{26}$$

where $\Lambda = \lambda/(a\sqrt{\epsilon_0})$, $\lambda = 2\pi/k_0$ is the wavelength of light in vacuum, and a is the distance between the nearest lattice sites.

Given the wave vectors $\mathbf{Q}$ and $\mathbf{Q}'$, Eqs. (24) and (25) yield

$$\begin{aligned} \zeta_x &= \sin\vartheta' \cos\varphi' - \sin\vartheta\cos\varphi, \\ \zeta_y &= \sin\vartheta' \sin\varphi' - \sin\vartheta\sin\varphi, \\ \zeta_z &= -(\cos\vartheta' + \cos\vartheta), \end{aligned} \tag{27}$$

the angles ϑ (ϑ') being counted from the positive (negative) direction of $\mathbf{e}_z$. When solved for the incidence angles ϑ, φ and the set (m_1, m_2, m_3) with, at least, one nonzero index m_i, Eq. (26) provides the angles ϑ', φ' that define the direction of the potentially allowed reflex (maximum of the diffraction intensity). Note that for the unit translations (A1) chosen, the indices (m_1, m_2, m_3) of diffraction reflex appeared in Eqs. (24) and (26) differ from the Miller indices (hkl) of the crystal plane perpendicular to the vector $\mathbf{b}$; this difference is clear from the relation (A4). The right-hand sides of Eqs. (26) are limited because of $|\zeta_{\alpha}| < 2$, i.e., the higher are the diffraction indices (m_1, m_2, m_3), the smaller is the $\lambda/(a\sqrt{\epsilon_0})$ ratio necessary for the diffraction to occur.

Next, we turn to Eq. (24) to analyze the Bragg diffraction kinematics for two fcc lattices that can appear in weakly disordered opal-like crystals. The displacement of a hcp layer from one of the above positions (A, B, or C) to the other two positions is provided by the interlayer unit translation $\hat{\mathbf{a}}_3$, which is either $\mathbf{t}_{\mathrm{I}}$ or $\mathbf{t}_{\mathrm{II}}$. If the translation is $\mathbf{t}_{\mathrm{I}}$ ($\mathbf{t}_{\mathrm{II}}$), a fcc …ABCABC… (…ACBACB…) lattice can arise, which will further be called a fcc-I (fcc-II) lattice. Unless otherwise stated, the fcc-I is referred to as the reference lattice, and the Miller indices of the planes and directions are given for this lattice.[36] In what follows, we will treat two incidence geometries relative to the reference fcc-I lattice presented in Fig. 2. In the case (i), the incident beam propagates along the (111) plane of the fcc-I structure, i.e. $\mathbf{Q}\parallel(111)$. In the case (ii), the beam incidence onto the (111) plane is oblique.

To proceed with the case (i), the vector $\mathbf{Q}\parallel(111)$ is assumed to make an angle ϕ with the direction $[\bar{2}11]$, as shown in Fig. 1(b). With the basis vectors (A2), one gets

$$\begin{aligned} \boldsymbol{\beta} = -\frac{2}{\sqrt{3}} \Bigg\{ & \mathbf{e}_x \left[m_1 \cos\left(\phi - \frac{\pi}{6}\right) + m_2 \sin\phi \right] \\ & + \mathbf{e}_z \left[m_1 \sin\left(\phi - \frac{\pi}{6}\right) - m_2 \cos\phi \right] \Bigg\} \\ & + \mathbf{e}_y \chi \left(m_3 - \frac{m_1 + 2m_2}{3} \right), \end{aligned} \tag{28}$$

on the right-hand side of Eq. (26), with the unit vectors $\mathbf{e}_z = \mathbf{Q}/Q$ ($\vartheta = 0$) and $\mathbf{e}_y \parallel [111]$. The parameter $\chi = a/A$ in Eq. (28) with the [111] interlayer spacing A enables one to treat a variety of structures, from a single layer ($A=\infty$, $\chi=0$) to a fcc lattice ($A_{\min} = a\sqrt{2/3}$, $\chi = \chi_{\max} = \sqrt{3/2}$).

For $\mathbf{Q}\parallel[\bar{2}11]$, when $\phi=0$, the first of Eqs. (26) with $m_1 = 0$ (i.e., $\zeta_x = 0$) has the solutions $\varphi'_1 = \pi/2$ and $\varphi'_2 = 3\pi/2$, which means that light is diffracted up and down the (111)

plane, respectively. The z projection of Eq. (26), $\zeta_z = 2m_2\Lambda/\sqrt{3}$, shows that at $m_1=0$ and $m_2=-1$ the Bragg diffraction with the wavelengths

$$\lambda(\vartheta') = \frac{a\sqrt{3\epsilon_0}}{2}(1+\cos\vartheta'), \tag{29}$$

occurs in the range $a\sqrt{3\epsilon_0}/2 < \lambda < a\sqrt{3\epsilon_0}$. Since the two equations are independent of χ, these are particularly valid for a single hcp layer ($\chi=0$). When dealing with the diffraction in a perfect 3D lattice, one should combine Eq. (29) with the rest of Eqs. (26), $\zeta_y = \Lambda\chi(m_3+2/3)$, to obtain

$$\tan\frac{\vartheta'}{2} = \frac{3}{2\sqrt{2}}\frac{1}{\sin\varphi'_{1,2}}\left(m_3+\frac{2}{3}\right), \tag{30}$$

for the reference fcc-I lattice ($\chi=\sqrt{3/2}$). The solutions of Eq. (30) are $\vartheta'_1 = 2\arctan(\sqrt{2}/2) = 70°30'$ and $\lambda(\vartheta'_1) = 2a\sqrt{\epsilon_0/3}$ for $m_3=0$ and $\sin\varphi'_1=1$; but they are $\vartheta'_2 = 2\arctan(\sqrt{2}/4) = 39°$ and $\lambda(\vartheta'_2) = (8/3)a\sqrt{\epsilon_0/3}$ for $m_3=-1$ and $\sin\varphi'_2=-1$. No other solutions are possible for the light diffracted by the fcc-I structure into the back hemisphere, or at $0<\vartheta'<\pi/2$ under the above conventions. At the other m_3 values, Eq. (30) gives solutions in the range of $\pi/2<\vartheta'<\pi$ (front hemisphere). The substitution of the obtained sets of integers m_i into Eq. (A4) brings one to the conclusion that the diffraction reflexes at $(\vartheta'_1,\varphi'_1)$ and $(\vartheta'_2,\varphi'_2)$ are due to the (200) and $(1\bar{1}\bar{1})$ planes, respectively. For the fcc-II structure, the related solutions to Eq. (30) $\tilde{\vartheta}'_1 = 39°$, $m_3=0$ at $\sin\varphi'_1=1$ and $\tilde{\vartheta}'_1 = 70°30'$, $m_3=1$ at $\sin\varphi'_2=-1$ [from the $(\bar{1}11)$ and $(\bar{2}00)$ planes] have mirror symmetry in respect to those of the fcc-I structure with (111) mirror plane.

Figure 3(a) presents the normalized structure factors $S_\perp^{\mathrm{I,II}}(\mathbf{q})/L$ calculated from Eq. (23) at $\mathbf{Q}\|[\bar{2}11]$ for the fcc-I and fcc-II lattices consisting of L hcp layers. Like the experimental data later, $S_\perp^{\mathrm{I,II}}(\mathbf{q})/L$ are plotted versus the registration angles $-90° < \Theta' < 90°$, where $\Theta' = -\vartheta'$ for the solution $\varphi'_2 = 3\pi/2$ and $\Theta' = \vartheta'$ for $\varphi'_1 = \pi/2$.[37] In the frame of the above kinematics analysis, the angular positions of the $S_\perp^{\mathrm{I}}(\mathbf{q})/L$ peaks at $\Theta'_1 = 70°30'$ and $\Theta'_2 = -39°$ [curve 1 in Fig. 3(a)] are due to the diffraction from the (200) and $(1\bar{1}\bar{1})$ planes of the reference fcc-I lattice. In turn, two maxima of curve 2 in Fig. 3(a) belong to the structure factor $S_\perp^{\mathrm{II}}(\mathbf{q})/L$ of the fcc-II lattice. Note that the Bragg wavelengths (29) are different for the $|\Theta'|=39°$ and $|\Theta'|=70°30'$ maxima. Besides, the sums $(S_\perp^{\mathrm{I}}+S_\perp^{\mathrm{II}})/(2L)$ presented by curves 3 and 4 in Fig. 3(a) estimate the structure factors for a mixture of alternating fcc-I and fcc-II structures having the same growth axis and equal numbers L of constituting layers. All the curves in Fig. 3(a) demonstrate a size effect in the broadening of the angular peaks $|\Delta\Theta'| \sim 1/L$, which becomes drastic at small L: $S_\perp^{\mathrm{I,II}}(\mathbf{q})/L \to 1$ at $L \to 1$.

Thus, we have discussed all processes potentially allowed in the backward diffraction, as these are defined by the structure factor normalized to unity. It follows from Eqs. (15) and (16), however, that the observable intensity of each peak is actually governed by the relevant form factor $|\delta\epsilon_{\mathbf{b}}|^2$. In particular, one can expect that the large-angle maxima of

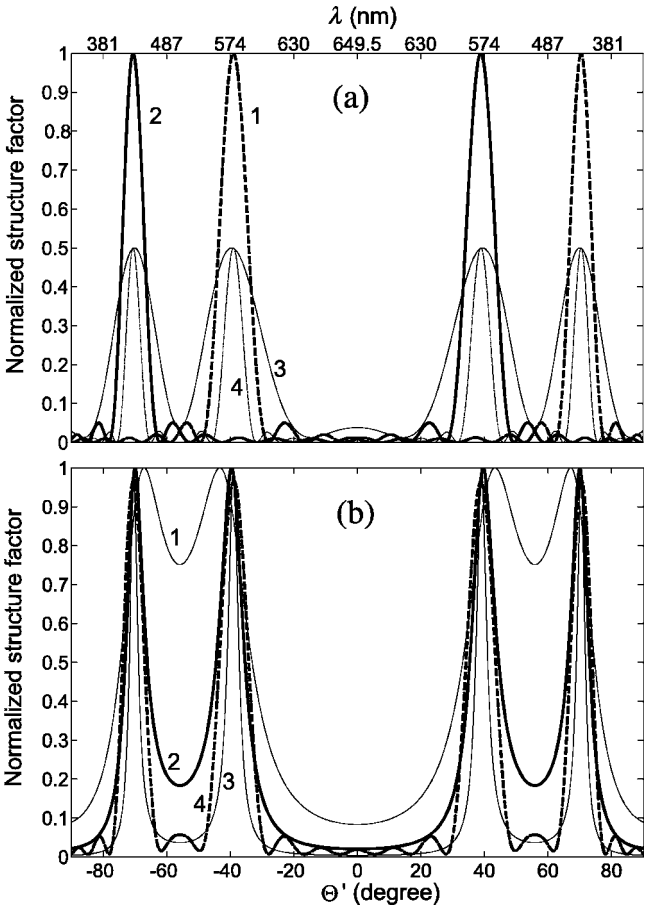

FIG. 3. The structure factors $S_\perp^{\mathrm{I,II}}/L$ calculated from Eq. (23) for the fcc-I and fcc-II lattices consisting of L hcp layers (a) and the normalized mean structure factor $\langle S_\perp\rangle$ of random stacking (b) as a function of the angle Θ' for the $\mathbf{Q}\|[\bar{2}11]$ incidence and $m_1=0$, $m_2=-1$. The $S_\perp^{\mathrm{I}}/L$ (curve 1) and $S_\perp^{\mathrm{II}}/L$ (2) are presented in panel (a) for $L=10$, and the sums $(S_\perp^{\mathrm{I}}+S_\perp^{\mathrm{II}})/(2L)$ are presented for $L=5$ (curve 3), and $L=15$ (4). The normalized values of $\langle S_\perp\rangle$ calculated from Eq. (39) are shown in panel (b) for the fcc packing probabilities $p=0.65$ (curve 1), $p=0.8$ (2), and $p=0.9$ (3). The upper wavelength scale corresponds to the Bragg condition (29). Panel (b) shows a good fit between the maxima of $\langle S_\perp\rangle$ at $p=0.8$ (curve 2) and $(S_\perp^{\mathrm{I}}+S_\perp^{\mathrm{II}})/L$ at $L=10$ (curve 4). Calculated at $a\sqrt{\epsilon_0}=375$ nm.

$S_\perp^{\mathrm{I,II}}(\mathbf{q})/L$ associated with the {200} planes will be suppressed.[21]

For comparison, we briefly consider the diffraction in the case (*ii*), i.e. under the oblique light incidence onto the (111) planes of the reference fcc lattice. The expression derived from Eq. (28) is

$$\boldsymbol{\beta}' = -\frac{2}{\sqrt{3}}\left\{\mathbf{e}'_x\left[m_1\cos\left(\phi-\frac{\pi}{6}\right)+m_2\sin\phi\right] + \mathbf{e}'_y\left[m_1\sin\left(\phi-\frac{\pi}{6}\right)-m_2\cos\phi\right]\right\} - \mathbf{e}'_z\chi\left(m_3-\frac{m_1+2m_2}{3}\right), \tag{31}$$

with $\mathbf{e}'_y \| [\bar{1}10]$ and $\mathbf{e}'_z \| [\bar{1}\bar{1}\bar{1}]$. At $m_1=m_2=0$, Eq. (26) with the substituted Eq. (27) and $\boldsymbol{\beta}'=-m_3\chi\mathbf{e}'_z$ following from Eq. (31) predicts a series of diffraction maxima under the Bragg condition

$$\lambda(\vartheta)=\frac{2}{m_3\chi}a\sqrt{\epsilon_0}\cos\vartheta, \tag{32}$$

where $m_3 \geqslant 1$. These correspond to specular reflection ($\vartheta'=\vartheta$ and $\varphi'=\varphi$) by the (111) planes of the reference fcc lattice, whose period a/χ is $d_{(111)}=a\sqrt{2/3}$. The lowest-order diffraction process with $m_3=1$ in Eq. (32) is just what has been extensively studied in the majority of reports on reflection[6,10,17,20,21] and transmission[6,8–10] in opals and related materials. The diffraction remains the same for the fcc-I and fcc-II lattices until the different diffraction processes with nonzero m_1 or m_2 become allowed. If the optical boundary defined by the function $\epsilon^0(z)$ is perpendicular to the [111] direction, the Bragg diffraction interferes the Fresnel reflection from the crystal surface.

In the next section, we consider how the diffraction features predicted above for fcc structures are modified by the growth-induced disorder typical of real opals.

D. Diffraction from randomly packed layers

We have pointed out above that opals and related photonic crystals are characterized by a probabilistic interchange of three possible positions (A, B, and C) of the hcp layers made up of a-SiO_2 spheres. This means that the translation vectors $\mathbf{t}_\mathrm{I}$ and $\mathbf{t}_\mathrm{II}$ in a 3D closely packed structure alternate in a random sequence. For this reason, the domains of the fcc-I lattice …ABCABC…, the fcc-II lattice …ACBACB…, and the 3D hcp lattice …ABABAB… coexist and alternate statistically along their common growth axis. For disordered opals, the structure factor in Eq. (20) appears on averaging the observable quantities (15) and (16). The mean structure factor entering Eq. (20) for random stacking of L hcp layers is the following:[38]

$$\langle S_\perp(\mathbf{q})\rangle=\sum_{l=-L+1}^{L-1}\left(1-\frac{|l|}{L}\right)\langle e^{-i\mathbf{q}\cdot\mathbf{R}_{0,l}}\rangle. \tag{33}$$

To evaluate Eq. (33), we introduce the fcc packing probability p, implying the event when two successive translations ($\mathbf{t}_\mathrm{I}$ or $\mathbf{t}_\mathrm{II}$) coincide in a random stack of hcp layers. There are the following possibilities: (1) a fcc-I or fcc-II lattice is formed, if $p=1$, (2) a 3D hcp lattice is formed, if $p=0$, and (3) a mixture of 3D hcp and fcc lattices appears, if $0<p<1$. In the latter case, the one-step mean phase factor $\langle e^{-i\mathbf{q}\cdot\mathbf{R}_{0,1}}\rangle=(1/2)\mathbf{e}^T\cdot\hat{M}(\mathbf{q})\cdot\mathbf{e}$ is defined by the matrix

$$\hat{M}(\mathbf{q})=\begin{pmatrix} pe^{-i\mathbf{q}\cdot\mathbf{t}_\mathrm{I}} & (1-p)e^{-i\mathbf{q}\cdot\mathbf{t}_\mathrm{II}} \\ (1-p)e^{-i\mathbf{q}\cdot\mathbf{t}_\mathrm{I}} & pe^{-i\mathbf{q}\cdot\mathbf{t}_\mathrm{II}} \end{pmatrix}, \tag{34}$$

where $\mathbf{e}$ is the vector matrix, whose transpose is $\mathbf{e}^T=(1,1)$ with $\mathbf{e}^T\cdot\mathbf{e}=2$. With account of

$$\langle e^{-i\mathbf{q}\cdot\mathbf{R}_{0,l}}\rangle=\frac{1}{2}\mathbf{e}^T\cdot\hat{M}^l(\mathbf{q})\cdot\mathbf{e} \tag{35}$$

at $l\geqslant 1$, Eq. (33) yields

$$\langle S_\perp(\mathbf{q})\rangle=\frac{1}{2}\mathbf{e}^T\cdot\left\{1+\sum_{l=1}^{L-1}\left(1-\frac{l}{L}\right)[\hat{M}^l+(\hat{M}^*)^l]\right\}\cdot\mathbf{e}. \tag{36}$$

Summing with the accuracy to the terms of the order $1/L \ll 1$ ($L\to\infty$) gives

$$\langle S_\perp(\mathbf{q})\rangle=\frac{1}{2}\mathbf{e}^T\cdot[(\hat{I}-\hat{M})^{-1}+(\hat{I}-\hat{M}^*)^{-1}-\hat{I}]\cdot\mathbf{e}, \tag{37}$$

where $\hat{I}$ is the unit matrix. Using in Eq. (37) the matrix (34) expressed through the vectors $\mathbf{t}_\mathrm{I}$ and $\mathbf{t}_\mathrm{II}$, we arrive at the relation

$$\langle S_\perp(\mathbf{q})\rangle=\frac{p(1-p)\sin^2\Delta\psi}{(1-2p)\sin^2\psi_0+p^2(1-2\cos\psi_0\cos\Delta\psi+\cos^2\Delta\psi)}, \tag{38}$$

where

$$\psi_0=\frac{1}{2}\mathbf{q}\cdot(\mathbf{t}_\mathrm{I}+\mathbf{t}_\mathrm{II}),\quad \Delta\psi=\frac{1}{2}\mathbf{q}\cdot(\mathbf{t}_\mathrm{I}-\mathbf{t}_\mathrm{II}),$$

and $\mathbf{t}_{\mathrm{I,II}}=(a/2)(\pm\hat{\mathbf{x}}/\sqrt{3}+\hat{\mathbf{y}}\sqrt{8/3}+\hat{\mathbf{z}})$ is taken in accordance with Eq. (A1).

Turning to the case (i) with the $\mathbf{Q}\|[\bar{2}11]$ incidence ($\vartheta=0$, $\phi=0$), we substitute into Eq. (38) the values of ζ_α for the solutions $\varphi'_1=\pi/2$ and $\varphi'_2=3\pi/2$ at $m_1=0$ and $m_2=-1$ with the Bragg condition (29). This yields the following structure factor averaged over the random stacking:

$$\langle S_\perp(\mathbf{q})\rangle=\frac{3}{2}\frac{p(1-p)}{(2p-1)(\cos 2\Phi-1)+p^2(2\cos\Phi+5/2)}, \tag{39}$$

where $\Phi=(4\pi\sqrt{2}/3)\tan(\Theta'/2)$. The normalized structure factors (39) for random stacks with different p values are presented in Fig. 3(b) as a function of the registration angle Θ' introduced in Fig. 3(a).[37] With increasing p, the angular dependence of $\langle S_\perp\rangle$ is seen to vary from the one typical of a 3D hcp lattice ($p\ll 1$) to that typical of fcc lattices ($1-p\ll 1$). This tendency has been derived from Fig. 3(b), though no limiting analytical expressions are available for Eq. (39). Curve 4 in Fig. 3(b) presents the sum $(S^\mathrm{I}_\perp+S^\mathrm{II}_\perp)/L$ at $L=10$ reproduced from Fig. 3(a). To compare, near the maxima this curve is very close to the normalized dependence $\langle S_\perp\rangle$ for $p=0.8$ presented by curve 2 in Fig. 3(b). Thus, the Θ' dependencies of $\langle S_\perp\rangle$ and $(S^\mathrm{I}_\perp+S^\mathrm{II}_\perp)/L$ derived, respectively, for the statistical and regular models of alternating fcc-I and fcc-II domains show good agreement.[38] To anticipate, such an alternation of domains indicates that opals do have a twinned fcc structure, the statement will be experimentally supported in Sec. V.

Before proceeding to the experiment, it is worthy commenting on a few important theoretical points. In the next sections the previous theory is demonstrated to explain all our experimental data on diffraction from real opals. Because our opal samples with $|\delta\epsilon_{\mathbf{b}_{(111)}}|/\epsilon_0 \approx 0.05$[39] are actually *low*-contrast dielectrics, it is not surprising that the discussed first-order solution of Eqs. (5), implying that $|\mathbf{E}-\mathbf{E}^0| \ll |\mathbf{E}^0|$ is exact enough. But if one has to deal with the optical diffraction from *high*-contrast photonic crystals, a question could arise about the role of effects occurring due to the interference of multiple-scattered waves. Such effects in the photonic crystal are taken into account by multiple-scattering numerical methods,[40] particularly applied to calculate optical diffraction-mediated transmission through colloidal crystals[22] and inverted opals.[32] These complicated numerical methods are mainly used to provide rich and detailed information about the photonic band structure,[41,42] represented as the dispersion branches of the frequency versus the wave vector covering the whole *volume* of the Brillouin zone of the lattice. In the Bragg diffraction essential are the processes associated with the *surface* of the Brillouin zone where the photonic stop bands open up. Given the diffraction channel $\mathbf{K} \rightarrow \mathbf{K}'$, such processes can be specified by either a single vector $\mathbf{b}$ or a few reciprocal lattice vectors simultaneously, the situations being referred to as single (presented here) or multiple Bragg diffraction,[21] respectively. In both cases, account of multiple-scattering effects could be taken by substituting a self-consistent solution of Eq. (6) rather than $\tilde{\mathbf{E}}^0$ in (5) and an analog of Eq. (13). Then, these get a resonant denominator whose zeros in the lowest-order approximation in $\delta\epsilon_{\mathbf{b}}$ define the conditions for the Bragg diffraction in a *perfect* crystal, providing the same diffraction intensity maxima as Eqs. (22)–(24). The higher-order corrections result in a complex term responsible for shift and broadening of the diffraction maxima, which optical effects can be treated semiempirically. In *real* crystals, imperfections and disorder of the lattice as well as finiteness of the crystal sizes are important origins of additional broadening of the Bragg maxima. Turning to our theory, it predicts significant broadening of single Bragg diffraction features due to stacking disorder and domain size effects (Fig. 3), under which conditions one may expect that the multiple-scattering effects will be suppressed.

III. OPAL STRUCTURE AND SAMPLE CHARACTERIZATION

The opal samples under study represented 3D closely packed structures with monodisperse spherical a-SiO_2 particles located at the lattice sites. The particle diameter was several hundreds of nanometers, i.e., its size was comparable with the wavelengths in the visible spectral region. The dielectric constant of the bulk amorphous silica is $\epsilon_{a\text{-}SiO_2} = 1.85$ (the refractive index $n_{a\text{-}SiO_2} \approx 1.36$), and the interparticle voids form a continuous network that can be filled with various liquids or solid materials. As an opal sample grows, silica particles form well-ordered hcp layers that successively stack to produce a 3D closely packed structure. We will assume further that the growing 2D hcp layers are parallel to the (111) plane of the reference fcc lattice, while the growth axis coincides with its [111] direction.

The details of the 3D closely packed structure will be discussed with reference to Fig. 2. We have mentioned in Sec. II that the hcp layers may occupy any of the three positions A, B, or C in the (111) plane. During the 3D stacking, any two adjacent layers may have any two different positions from the set A, B, and C. The resulting periodic layer sequence …ABCABC… produces a fcc lattice, whereas the sequence …ABABAB… forms a 3D hcp lattice. A random layer sequence, say, …ABACBACA…, provides a 3D closely packed structure disordered along the normal to the layers. Among the 1D disordered structures that appear during the growth, we will single out a twinned …ACB*A*BCA… structure, well known from crystallography, which is made up of two fcc lattices (fcc-I and fcc-II in Fig. 2) having a common plane denoted as *A*. It is important for further discussion that the (111), and $(\bar{1}\bar{1}\bar{1})$ growth planes in synthetic opals are physically different from the other six planes, i.e., from the $(\bar{1}11)$, $(1\bar{1}1)$, $(11\bar{1})$, $(\bar{1}\bar{1}1)$, $(\bar{1}1\bar{1})$, and $(1\bar{1}\bar{1})$ planes that would be equivalent to the (111) planes in the perfect fcc lattice. This is due to the random stacking of hcp layers along the [111] growth axis. As a result, the [111] and $[\bar{1}\bar{1}\bar{1}]$ axes appears to be different from the $[\bar{1}11]$, $[1\bar{1}1]$, $[11\bar{1}]$, $[\bar{1}\bar{1}1]$, $[\bar{1}1\bar{1}]$ and $[1\bar{1}\bar{1}]$ axes that change their direction with the transition from a fcc-I domain to a fcc-II domain, and vice versa. This is illustrated in Fig. 2, showing that the arrangement of sites in the hcp layers formed by a-SiO_2 particles in the (111) or $(\bar{1}\bar{1}\bar{1})$ planes is perfectly ordered, while in the other planes of the {111} family the sphere packing is irregular due to a random alternation of domains of the fcc-I and fcc-II lattices along the [111] growth axis.

Our study was performed with well characterized and oriented opal samples, as described previously.[12,26] The samples were a few centimeters at the base and about 1 cm high. Atomic-force microscopy was used to match the crystal axes with the geometry of each sample and to determine the lattice parameters. In order to visualize the Bragg diffraction in the visible wavelength range, we selected samples with silica spheres having an average diameter $D \approx 270$ nm.

The analysis of the optical transmission spectra showed that the sample structure essentially changed along the growth axis.[15] The sample regions at the initial growth stage manifested a strong structural disorder that manifested itself, among other things, as a disorientation of some crystallites relative to the sample growth axis. The best structural perfection was achieved at the latest growth stage. The atomic-force micrographs demonstrated a long range ordering of a-SiO_2 spheres in the 2D hcp layers on the scale of a few hundreds of microns.[15] In the present study we analyzed the diffraction patterns of various regions of the initial sample, both strongly disordered and best ordered ones.

IV. EXPERIMENTAL TECHNIQUES

A. Experimental setup

The diffraction experiments on synthetic opals were carried out using a setup shown schematically in Fig. 4. For

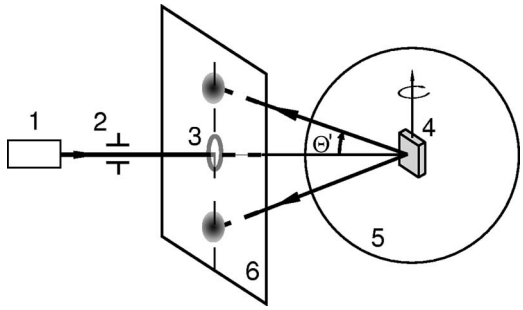

FIG. 4. Experimental setup: light source (1), collimator (2), focusing lens (3), opal sample (4), spherical vessel (5), semitransparent screen (6). The diffraction pattern shown schematically on the screen is for a monochromatic light beam incident along $[\bar{2}11]$ in the (111) growth plane.

monochromatic illumination, we employed Ar^+, He-Ne, and Cu lasers or an incandescent lamp as a source of white light (1). In the latter case, the light beam was collimated with a diaphragm and a lens (2). An additional focusing lens (3) with the focal length of 6 cm was used to reduce the light spot on the sample. An opal sample (4) was fixed at the center of a spherical cell (5) of 5 cm in diameter, filled with glycerin (the dielectric constant $\epsilon_{gl}=2.07$, the refractive index $n_{gl}=1.44$) and used as an immersion medium to suppress diffusive light scattering from the surfaces. According to Eq. (2), the effective dielectric constant of an opal sample is $\epsilon_0=0.74\epsilon_{a\text{-}SiO_2}+0.26\epsilon_{gl}\approx 1.91$ ($n_0=\sqrt{\epsilon_0}\approx 1.38$, in which case $a\sqrt{\epsilon_0}\approx 375$ nm for our samples with the above constant $\epsilon_{a\text{-}SiO_2}\approx 1.85$). As a result, there was practically neither reflection nor refraction of light on the sample surface, and the effects of the sample shape and surface morphology were negligible, which allowed making quantitative measurements of the spectral and angular dependencies of the diffracted light intensities. The crystallographic axes were oriented along the axis of a scaled circle that could be precisely rotated. A translucent frosted glass screen (6) with a mounted focusing lens (3) was placed in between the light source and the sample. The screen was used to register the light diffracted by the sample (4) to the back hemisphere. The diffraction patterns were visualized on the screen, photographed and analyzed by a DFS-24 spectrometer that received the signal through an optical fiber.

B. Diffraction geometries

The diffraction experiments registered (at a high angular resolution) the intensity of light scattered into the large solid angle of the back hemisphere. To observe the most representative diffraction patterns, we employed two geometries of light incidence with respect to the opal structure (Fig. 2). The geometry denoted as (*i*) in Sec. II C corresponds to the wave incidence along the (111) layers, i.e., perpendicularly to the [111] growth axis. The other geometry, denoted as (*ii*), corresponds to the normal or oblique incidence on the (111) growth plane. The two situations cover all incidence geometries for opal crystal structures.

Here we focus on the most informative (*i*) geometry,

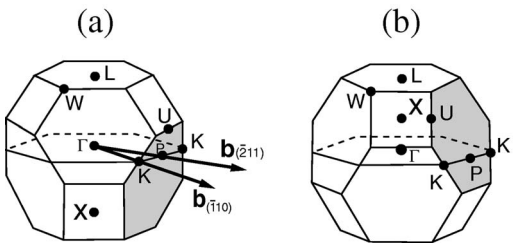

FIG. 5. The Brillouin zones of the fcc-I (a) and fcc-II (b) structures that form a twin.

which has not been considered in detail before. The incident beam propagates along the 111 growing layers. Since these layers have a hexagonal symmetry, we can identify two major high symmetry directions of the wave vector $\mathbf{Q}\|(111)$ of the incident beam [Fig. 1(b)]. In one case, the beam with $\mathbf{Q}\|[\bar{1}10]$ is incident along continuous chains of closely packed a-SiO_2 spheres in the (111) hcp layer [Fig. 1(b)]. This orientation corresponds to the Γ-K direction in the Brillouin zone of the reference fcc-I lattice [Fig. 5(a)]. In the other case, the $\mathbf{Q}\|[\bar{2}11]$ beam is normal to the chain of silica spheres making the angle of 60° with the $\mathbf{Q}\|[\bar{1}10]$ beam [Fig. 1(b)]. The $\mathbf{Q}\|[\bar{2}11]$ incidence corresponds to the Γ-P direction in the reciprocal space. The untabulated symbol P has been introduced for the point of interception of the $\mathbf{b}_{(\bar{2}11)}\|[\bar{2}11]$ vector of the reciprocal lattice and the Brillouin zone surface. It should be emphasized that the angle between the $[\bar{1}10]$ and $[\bar{2}11]$ directions is 30° [Fig. 1(b)] and that owing to the symmetry of the hcp layers, exhaustive information on the diffraction in the (*i*) geometry can be obtained by varying the $\mathbf{Q}\|(111)$ vector within this angle.

In the (*ii*) geometry, we observed on the screen a single bright diffraction spot in the direction of the specular reflection relative to the [111] normal.[43] This spot satisfies the condition (32) with $m_1=m_2=0$ and $m_3=1$ for the Bragg diffraction from a sequence of (111) hcp layers. The [111] lattice period was $a\sqrt{2/3}=220$ nm in our samples, with $a=D$, because of the close packing of the a-SiO_2 spheres. Note that this type of Bragg reflection of light from the (111) growth surface has been a subject of detailed analysis in many experiments on angle-resolved reflection.[6,10,17,20,21,43]

V. RESULTS AND DISCUSSION

Since our experiments were performed with opals immersed in a liquid filling a spherical vessel, we will not distinguish between the wave vectors in the sample, in the immersion liquid and outside the vessel, for which reason we assume $\mathbf{K}\approx\mathbf{Q}$, $\mathbf{K}'\approx\mathbf{Q}'$ and $\epsilon_1\approx\epsilon_0$ in applying the previous theory (Sec. II) to our experiments. According to Eq. (24) and Fig. 1(a), the directions of the principal diffraction maxima are defined by the kinematic relations $\mathbf{Q}'-\mathbf{Q}=\mathbf{b}_{(hkl)}$ with $|\mathbf{Q}'|=|\mathbf{Q}|$.

A. Diffraction in the $\mathbf{Q}\|[\bar{2}11]$ geometry

To start, we discuss the experimental data on the $\mathbf{Q}\|(111)$ geometry with the analysis of diffraction patterns of samples

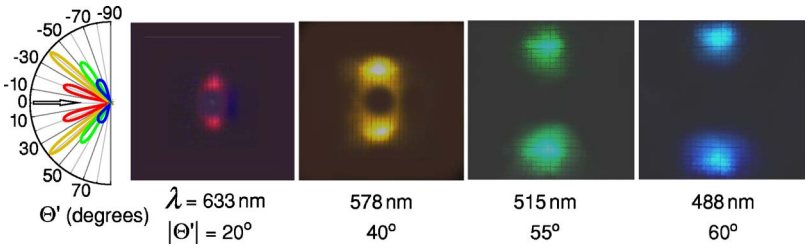

FIG. 6. (Color online) Photographs of diffraction patterns on the screen for the $[\bar{2}11]$ incidence of monochromatic light with the wavelengths $\lambda = 633$, 578, 515, and 488 nm and the respective registration angles $|\Theta'|$.

illuminated with monochromatic or white light along the $[\bar{2}11]$ direction (Fig. 5). If the number of alternating fcc-I and fcc-II fragments (domains of random thickness) is large, it means the existence of a multiplicity of twins located randomly along the [111] growth axis normal to them. Each perfect fcc-I and fcc-II lattice has its own Brillouin zone shown in Figs. 5(a) and 5(b), respectively. One can notice that one zone changes to the other either in the mirror reflection in the (111) plane of the reference fcc lattice or when it is rotated through 60° around its [111] axis. The $\mathbf{Q}\|[\bar{2}11]$ light beam propagates along the (111) growth plane common to both fcc lattices (Fig. 2). The beam width usually appears to be larger than the characteristic size of the fcc-I and fcc-II domains, and the typical diffraction pattern contains two spots symmetric with respect to the (111) plane. The angular deviation $|\Theta'|$ of the spot centers increases with decreasing wavelength. This is illustrated in the photographs in Fig. 6, taken in monochromatic light with various wavelengths.

To interpret these patterns, we should remember that if a monochromatic beam is incident on a twinned fcc structure along the $[\bar{1}10]$ direction, the Bragg reflection $\mathbf{Q}\rightarrow\mathbf{Q}'$ into the back hemisphere shown for the fcc-I lattice in Fig. 2 is allowed for several sets of {111} planes. In order to identify these planes, we should keep in mind that diffraction from the $(h'k'l')$ crystal plane into the back hemisphere relative to the light incidence direction $\mathbf{Q}$ is generally allowed, if $\Omega_{[hkl]}^{[h'k'l']} > 135°$, where $\Omega_{[hkl]}^{[h'k'l']}$ is the angle between the $\mathbf{Q}\|[hkl]$ direction and the normal $[h'k'l']\|\mathbf{b}_{(h'k'l')}$ to the set of $(h'k'l')$ planes responsible for the diffraction. If $\Omega_{[hkl]}^{[h'k'l']} < 135°$, the diffracted beam will face the front hemisphere and propagate into the sample. For this reason, the $\mathbf{Q}\|[\bar{2}11]$ monochromatic diffraction into the back hemisphere will be allowed only for the $(1\bar{1}\bar{1})$ plane with $\Omega_{[\bar{2}11]}^{[1\bar{1}\bar{1}]} \approx 160°$ out of the eight {111} planes, and the Bragg angle will then be $|\Theta'| \approx 39°$ (Fig. 4). The $(\bar{1}11)$ planes of the fcc-II structure make a similar contribution to the diffraction. Therefore, the $\mathbf{Q}\|[\bar{2}11]$ geometry gives *two* diffraction spots at $\Theta' = \pm 39°$ that are symmetric with respect to the (111) plane because of the diffraction from the {111} planes of the fcc-I and fcc-II lattices. For our samples with $D \approx 270$ nm, the Bragg condition (29) is fulfilled for light with $\lambda_B = 565$ nm.

It should be noted that the *two* spots were observed experimentally both at the theoretical Bragg angle $|\Theta'| = 39°$ and wavelength $\lambda_B = 565$ nm and at the other values of Θ' and λ (Fig. 6). To explain this result, we carried out experiments on diffraction of white light with $\mathbf{Q}\|[\bar{2}11]$. We observed on the screen a color strip along the [111] growth axis. The spectral structure of the strip was analyzed in detail as a function of Θ' (this angle was varied by moving the optical fiber, transmitting the diffracted light to a spectrometer). The angle-resolved reflectivity spectra measured at various registration angles Θ' are presented in Figs. 7(a) and 7(b).[37] The spectra in Fig. 7(a) are for the light scattered into the lower region of the back hemisphere in the range $-60° < \Theta' < 0$, while those in Fig. 7(b) are for the scattering into the upper region of the same hemisphere in the symmetric range $0 < \Theta' < 60°$. Figure 7(c) shows the intensity variation at the peaks of the reflection bands presented in Figs. 7(a) and 7(b).

It is clear from Fig. 7 that the diffraction pattern represents the spectral dispersion of white light along two symmetric directions relative to the incident beam, producing a symmetric iridescent strip. For the strip, the spectral width is

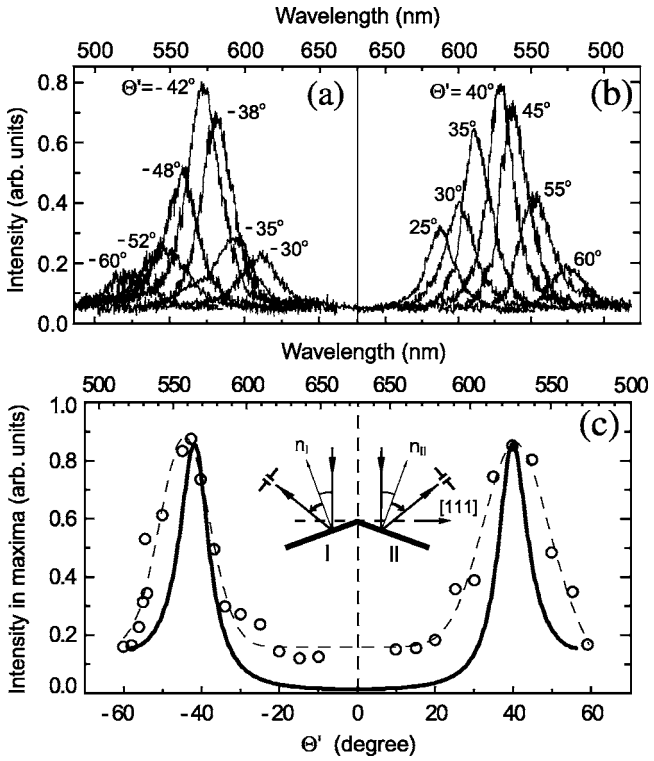

FIG. 7. (a), (b) Diffraction spectra registered at various angles Θ' for white light incident on the sample along the $[\bar{2}11]$ direction. (*c*) The spectral angular dependence of the light intensity at the scattering peaks shown in (*a*) and (*b*): circles and dashed line—experimental data; solid line—calculations. The insert shows the geometry of light scattering by two sets of $(1\bar{1}\bar{1})$ planes in the fcc-I and fcc-II lattices of a twinned fcc structure.

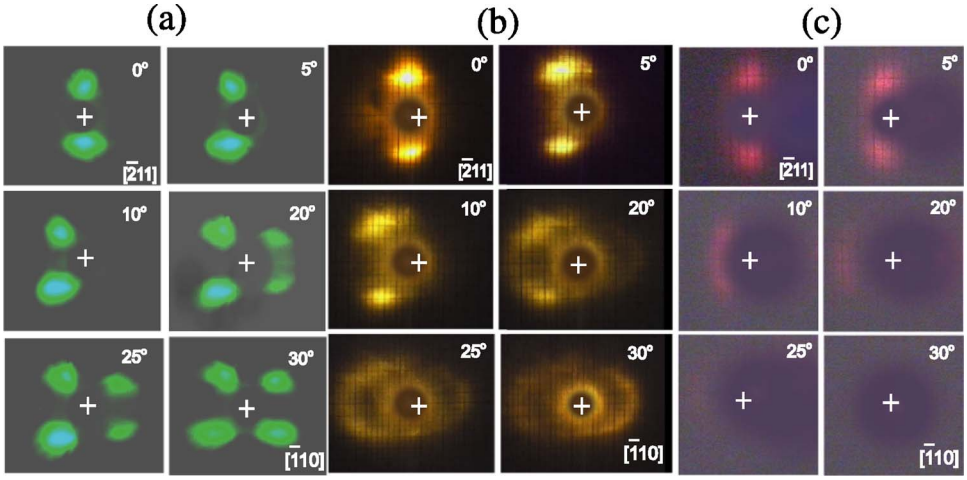

FIG. 8. (Color online) Observed transformation from *two*- to *four*-spot diffraction patterns in varying the sample rotation angle ϕ from $\phi=0$ (the $\mathbf{Q}\|[\bar{2}11]$ incidence) to $\phi=30°$ ($[\bar{1}01]$ incidence). The patterns were registered in monochromatic light at the following wavelengths: 515 nm (a), 578 nm (b), and 633 nm (c). The sample was oriented so that the growth axis [111] is normal to the incident beam.

about 150 nm and the angular width is $\approx 20°$. The angular dispersion agrees well with Eq. (29), which yields the dispersion relation $\lambda(\Theta')=(D\sqrt{3\epsilon_0}/2)(\cos\Theta'+1)$ for $\mathbf{Q}\|[\bar{2}11]$, indicating that the Bragg wavelength λ decreases with increasing $|\Theta'|$. Our sample with $D\approx 270$ nm reflected red light into the back hemisphere at a small angle ($\Theta'\to 0$), with the wavelength of the strictly backscattered light ($\Theta'=0$) being $\lambda(0)=D\sqrt{3\epsilon_0}=650$ nm.

Let us compare the experimental angular dependence of the white light diffraction intensity and the results derived from the scattering theory presented in Sec. II D, with reference to randomly packed hcp layers. In addition to the experimental diffraction intensity, Fig. 7(c) shows the relationship between the normalized averaged structure factor $\langle S_\perp\rangle$ given in Fig. 2(b) and the registration angle Θ', which provides the best fit with the experiment. It is clear from Fig. 7 that the white light pattern has two well-defined intensity peaks at $\Theta'\approx\pm 40°$ when the beam is incident along the $[\bar{2}11]$ direction, with the absolute maximum at $\lambda\approx 570$ nm. These values fit perfectly well the Bragg values of $|\Theta'|=39°$ and $\lambda_B=565$ nm for the averaged structure factor maxima. The theoretical normalized $\langle S_\perp\rangle$ curve in Fig. 7(c) was plotted for the fcc packing probability $p=0.8$.

Thus, the analysis of the angular dependence of the diffraction intensity (the structure factor $\langle S_\perp\rangle$) in the $\mathbf{Q}\|[\bar{2}11]$ geometry, which we have made in terms of the theory developed in Sec. II D, has provided the fcc packing probability $p=0.8$ to describe the interlayer disorder in the samples we studied. On the other hand, the close agreement between the theoretical dependences $\langle S_\perp\rangle$ at $p=0.8$ and $(S_\perp^I+S_\perp^{II})/L$ at $L=10$, presented in Fig. 3(b), means that the characteristic number of hcp layers in the fcc-I and fcc-II domains in our opal samples is $\bar{L}\sim 10$. This conclusion is supported by our calculations of the average fcc domain length, made using the theoretical distribution function of hcp layers over domains of different lengths. As for a detailed analysis of random fcc twins in opals, it is a probabilistic problem to be treated elsewhere.

B. Diffraction in the $\mathbf{Q}\|[\bar{1}10]$ geometry

Consider light diffraction in opals when the incident beam propagates along another highly symmetric direction in the (111) growth plane, i.e., along chains of a-SiO_2 spheres (the $\mathbf{Q}\|[\bar{1}10]$ geometry, the Γ-K direction), Fig. 5. For the reference fcc-I lattice, the condition for the diffraction in the back hemisphere at $\Omega_{[hkl]}^{[h'k'l']}>135°$ is valid for two sets of {111} planes: $(1\bar{1}1)$ and $(1\bar{1}\bar{1})$. For these planes the angles $\Omega_{[hkl]}^{[h'k'l']}$ are identical: $\Omega_{[\bar{1}10]}^{[1\bar{1}1]}=\Omega_{[\bar{1}10]}^{[1\bar{1}\bar{1}]}=144°40'$. The contribution to the diffraction from the $(\bar{1}1\bar{1})$ and $(\bar{1}11)$ planes of the fcc-II structures is similar. Therefore, there should be *four* diffraction spots due to the diffraction from the {111} planes of the fcc-I and fcc-II domains in the $\mathbf{Q}\|[\bar{1}10]$ geometry. In the opals with the a-SiO_2 sphere diameter $D\approx 270$ nm, the Bragg condition is satisfied at $\lambda_B\approx 500$ nm.

Indeed, the $\mathbf{Q}\|[\bar{1}10]$ experiments showed *four* spots at certain λ values, which were located at the vertices of a rectangle with two sides parallel to the [111] axis. The four-spot pattern from the samples with $D\approx 270$ nm is clearly visible when monochromatic light has $\lambda=515$ nm, as shown in Fig. 8(a). But at $\lambda=578$ and 633 nm, there is no four-spot pattern [Figs. 8(b) and 8(c)] because the λ values differ much from the Bragg value, an issue to be discussed later.

C. General features of $\mathbf{Q}\|(111)$ diffraction

Here we will analyze diffraction patterns of monochromatic light incident on a sample with the wave vector $\mathbf{Q}\|(111)$ making different angles ϕ with the $[\bar{2}11]$ direction in the (111) plane [Fig. 1(b)]. This experiment was made by rotating the sample around its [111] growth axis, as shown in Fig. 4. Since the immersion liquid had a dielectric permittivity close to that of opal (see Sec. III A), the stray scattering from the rough surface and specular reflection due to the presence of a background dielectric permittivity were considerably reduced. As a result, the diffraction patterns were practically independent of the sample shape and did not change while the beam scanned the surface of a pretreated high quality sample, in which the orientation of the fcc crystallographic axes were fixed with respect to the incident beam. The patterns changed only with the sample rotation angle $-\phi$ relative to the wave vector $\mathbf{Q}$ in the (111) plane of hcp layers [Fig. 1(b)]. Since the vessel (5) containing the

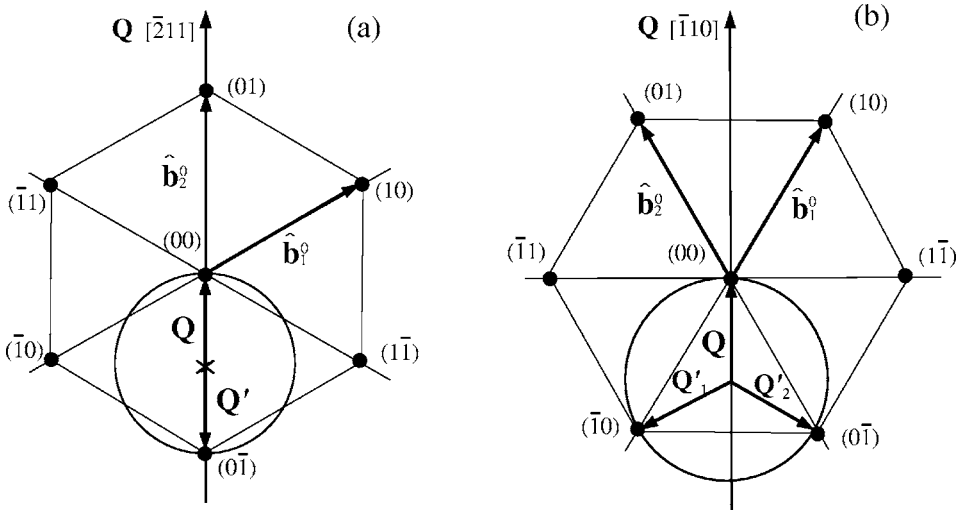

FIG. 9. The Ewald constructions for diffraction from a single hcp layer for the incidence geometries $\mathbf{Q}\|[\bar{2}11]$ (a) and $\mathbf{Q}\|[\bar{1}10]$ (b) with the light wave vectors related to the reference fcc lattice. The basis vectors $\hat{\mathbf{b}}_1^0$ and $\hat{\mathbf{b}}_2^0$ of the reciprocal lattice are calculated from Eq. (A3). The pair (m_1m_2) of site indices specify a diffraction reflex.

sample was spherical (Fig. 4), there was no pattern distortion because of the refraction of the diffracted light at the liquid-wall-air interfaces.

1. Pattern evolution during the sample rotation

Consider first the patterns obtained in monochromatic light with $\lambda=515$ nm [Fig. 8(a)]. We have shown in Secs. V A and V B that there are *two* spots located on the screen along the [111] growth axis of a twinned fcc structure in the $\mathbf{Q}\|[\bar{2}11]$ geometry at $\phi=0$. However, the number of spots increases to *four* in the $\mathbf{Q}\|[\bar{1}10]$ geometry with $\phi=-30°$. As the sample is rotated around its [111] axis from the $[\bar{1}10]$ incidence direction to the $[\bar{2}11]$ one, we observe a continuous transformation from a four-spot to a two-spot pattern. When the sample is rotated through 30° from $[\bar{2}11]$ to $[\bar{1}01]$, the two-spot pattern changes to the four-spot one in the reverse order. Then this transformation is repeated periodically with each 60° rotation. It is essential that a perfect fcc lattice has the symmetry axis $C_3\|[111]$ seen in Fig. 1(b), so that the patterns of a monodomain lattice should be repeated every time the rotation angle appears to be multiple to 120°.

The way the diffraction patterns evolve with the sample rotation around the [111] axis from $[\bar{2}11]$ to $[\bar{1}01]$ is strongly dependent on the light wavelength. If the incident beam propagates along the $[\bar{2}11]$ direction, *two* beam-symmetric spots are observed at all of the above wavelengths. At $\lambda=515$ nm, the diffraction spots are observed in the angle range $-30° \leqslant \phi \leqslant 30°$. At $\lambda=578$ nm, there are spots only at $-20° \gtrsim \phi \gtrsim 20°$ [Fig. 8(b)], and there is no *four*-spot pattern. Finally, when the incident light has $\lambda=633$ nm, two spots are observed in a still smaller range of the rotation angle, $-10° \gtrsim \phi \gtrsim 10°$ [Fig. 8(c)].

In order to explain the observed effects of appearance, displacement and quenching of the diffraction spots with changing rotation angle ϕ, let us turn to Eqs. (26)–(28) for $\mathbf{Q}\|(111)$ at $\vartheta=0$. If we divide the scattering vector $\mathbf{q}=\mathbf{q}_\parallel+\mathbf{q}_\perp$ into the in-plane $\mathbf{q}_\parallel\|(111)$ and perpendicular $\mathbf{q}_\perp$ components, the former can be derived from Eqs. (26)–(28) as

$$\sin\vartheta'\cos\varphi' = -\frac{2\Lambda}{\sqrt{3}}\left[m_1\cos\left(\phi-\frac{\pi}{6}\right)+m_2\sin\phi\right],$$

$$1+\cos\vartheta' = \frac{2\Lambda}{\sqrt{3}}\left[m_1\sin\left(\phi-\frac{\pi}{6}\right)-m_2\cos\phi\right]. \quad (40)$$

Consistent with the two equations is the normal component

$$q_\perp/(k_0\sqrt{\epsilon_0}) = \sin\vartheta'\sin\varphi', \quad (41)$$

defined by the 3D packing of the hcp layers. Formally, Eqs. (40) coinside with the equation $\mathbf{q}_\parallel=m_1\hat{\mathbf{b}}_1^0+m_2\hat{\mathbf{b}}_2^0$ for the in-layer Bragg diffraction with the wave vectors $\mathbf{Q}\|(111)\|\mathbf{Q}'$ by a single hcp layer, whose reciprocal lattice vectors $\hat{\mathbf{b}}_1^0$ and $\hat{\mathbf{b}}_2^0$ are defined by Eq. (A3) in the Appendix. For this reason, we first analyze the Bragg diffraction within the model of a single hcp layer.

2. Diffraction from a single layer

For the reference fcc structure, the diffraction equations (40) at $\mathbf{Q}\|[\bar{2}11]$ ($\phi=0$) for the pair of indices $m_1=0$, $m_2=-1$ give the solutions

$$\lambda^{[\bar{2}11]}(\Theta') = \frac{a\sqrt{3\epsilon_0}}{2}(1+\cos\Theta'); \quad \varphi_1'=\pi/2, \quad \varphi_2'=3\pi/2, \quad (42)$$

written in terms of the experimental registration angle $-90°<\Theta'<90°$, which is $\Theta'=-\vartheta'<0$ at $\varphi_2'=3\pi/2$ and $0<\Theta'=\vartheta'$ at $\varphi_1'=\pi/2$.[37] The solution (42) is designated by the point $(0\bar{1})$ in the 2D Ewald scheme shown in Fig. 9(a) for a hcp layer with the reciprocal lattice vectors $\hat{\mathbf{b}}_1^0$ and $\hat{\mathbf{b}}_2^0$ from Eq. (A3). It follows from Eq. (42) that the diffracted beam of white light with $\mathbf{Q}\|[\bar{2}11]$ should give an iridescent strip on the screen, as shown by the dashed line A in Fig. 10. The wavelengths are dispersed in Θ' symmetrically from the screen center up (along the ray $\varphi_1'=\pi/2$) and down (along the ray $\varphi_2'=3\pi/2$), following the Bragg condition (42).

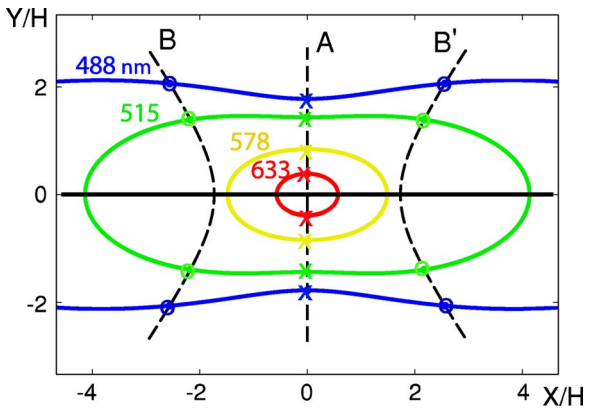

FIG. 10. (Color online) The on-screen trajectories of monochromatic spots (at 488, 515, 578, and 633 nm wavelengths) in diffraction from the hcp layer (solid lines), calculated as a function of the layer rotation angle ϕ around the layer normal in the range $-30° < \phi < 30°$, Fig. 1(b). Dashed lines present the theoretical strip A at $\phi=0$ ($\mathbf{Q}\|[\bar{2}11]$ incidence relative to the reference fcc lattice), the arc B at $\phi=-30°$ ($\mathbf{Q}\|[\bar{1}10]$), and the arc B′ at $\phi=30°$ ($\mathbf{Q}\|[\bar{1}01]$). The on-screen coordinates X and Y are calculated using Eqs. (40) for the diffraction into the back hemisphere with $a\sqrt{\epsilon_0}=375$ nm and the sample-to-screen distance H was 6 cm in our experiment.

To compare, for $\mathbf{Q}\|[\bar{1}10]$ ($\phi=-30°$), Eqs. (40) for the diffraction reflex with $m_1=-1$, $m_2=0$ and $m_1=0$, $m_2=-1$ result in $\sin\vartheta'\cos\varphi'=\pm\Lambda/\sqrt{3}$ and $1+\cos\vartheta'=\Lambda$. Here the signs $\pm$ correspond, respectively, to the points $(\bar{1}0)$ and $(0\bar{1})$ in the Ewald scheme in Fig. 9(b). The solutions of the related equations

$$\lambda^{[\bar{1}10]}(\Theta')=a\sqrt{\epsilon_0}(1+\cos\Theta'),\quad \cos\varphi'=\frac{1}{\sqrt{3}}\cot\frac{\Theta'}{2}, \tag{43}$$

exist only at $60°<|\Theta'|<90°$. At $|\Theta'|_{\min}=60°$, Eq. (43) yields $\varphi_1'=0$ and $\varphi_2'=\pi$ for the above reflexes $(\bar{1}0)$ and $(0\bar{1})$ registered at the wavelength $\lambda_{\max}^{[\bar{1}10]}=3a\sqrt{\epsilon_0}/2$. Above $|\Theta'|_{\min}$, the solution $\varphi_1'=0$ splits into $\bar{\varphi}'$ and $2\pi-\bar{\varphi}'$, while $\varphi_2'=\pi$ splits into $\pi\mp\bar{\varphi}'$ with $\bar{\varphi}'=\arccos[3^{-1/2}\cot(|\Theta'|/2)]$. At $|\Theta'|\to 90°$, the four solutions (reflexes) go to asymptotes with $\bar{\varphi}'(90°)=\arccos(1/\sqrt{3})\approx 54°45'$ and $\lambda^{[\bar{1}10]}\to a\sqrt{\epsilon_0}$. The calculation shows that the $\mathbf{Q}\|[\bar{1}10]$ diffracted beam of white light should produce the iridescent arcs B and B′ on the screen. These are shown by dashed lines in Fig. 10, the colors (wavelengths) change symmetrically away from the screen center, in accordance with Eq. (43). It follows from Eqs. (40) that the arcs B ($\phi=-30°$) and B′ ($\phi=30°$) and the strip A ($\phi=0$) are reproduced when the angle ϕ rotates through 60° with the reflex indices (m_1m_2), given by the Ewald scheme (Fig. 9). These color lines can be observed for a single hcp layer because its structure factor (23) at $L=1$ is $S_\perp(\mathbf{q})=1$, and any of the vector components (41) is allowed because of $\mathbf{b}_3^0=0$ according to Eq. (A3). When a restriction is imposed on the vector $\mathbf{q}_\perp$, these lines (A,B,B′) serve as a basis to form diffraction spots.

When a single hcp layer is illuminated by monochromatic light, the color spots with the given wavelength λ are expected to be selected from the strip A and the arcs B and B′. In the reference $\mathbf{Q}\|[\bar{2}11]$ geometry, for example, the above two spots $\varphi_1'(\Theta')$ and $\varphi_2'(\Theta')$ appear on the screen at the angle Θ' defined by Eq. (42). When the rotation angle ϕ changes continuously, say, in the range $-30°\leqslant\phi\leqslant 30°$, the two colored spots change their positions on the screen, moving along certain lines. The spot trajectories calculated at the laser wavelengths λ=488, 515, 578, and 633 nm used in our experiments are shown in Fig. 10 in the coordinates on a plane screen $(X,Y)=H(\cos\varphi',\sin\varphi')\tan\Theta'$, where H is the sample-to-screen distance. It is seen that some trajectories (λ=488, 515 nm) intersect the strip and arcs, the latter intersections indicating the appearance of four spots at $\mathbf{Q}\|[\bar{1}10]$ ($\phi=-30°$). The trajectories of the spots at λ=578 and 633 nm have no common points with the arcs B and B′, i.e., there is no diffraction in the $\mathbf{Q}\|[\bar{1}10]$ and $\mathbf{Q}\|[\bar{1}01]$ geometries. When the rotation angle varies from $\phi=0$ ($\mathbf{Q}\|[\bar{2}11]$ incidence) to $\phi=+30°$, $\mathbf{Q}\|[\bar{1}01]$, Fig. 1(b), (or $\phi=-30°$, $\mathbf{Q}\|[\bar{1}10]$) the 633 nm spots disappear at a much smaller deviation of ϕ than the 578 nm spots.

We have mentioned that the color lines A, B, and B′ were observed in our experiments, but the intensity distribution measured along the lines was found to be essential in a rather narrow wavelength range. It is easy to see that the displacements of diffraction spots during the sample rotation (Fig. 8) fit well the trajectories of the points calculated for a single layer at a given wavelength (Fig. 10). Thus, the results obtained within the diffraction theory describe well the whole combination of diffraction patterns arising at the variation of the light wavelength and the sample rotation angle.

D. Long-wavelength diffraction edges

For the Bragg wavelength of diffraction reflex $(\mathbf{m})=(m_1,m_2,m_3)$ in a 3D lattice, Eqs. (24) with $|\mathbf{Q}'|=|\mathbf{Q}|=\sqrt{\epsilon_0}\omega/c$ yield

$$\lambda^{[hkl]}(\mathbf{m},\vartheta)=4\pi\sqrt{\epsilon_0}\left[\sum_{i,j}m_im_j(\hat{\mathbf{b}}_i\cdot\hat{\mathbf{b}}_j)\right]^{-1/2}\cos\vartheta, \tag{44}$$

where $\pi-\vartheta$ is the angle between the vectors $\mathbf{Q}$ and $\mathbf{b}$ from Eq. (24). Note that the Miller indices $[hkl]$ are expressed thought the above reflex indices (m_1,m_2,m_3) using Eq. (A4). The above experimental data have revealed a maximum value of diffraction wavelength for each incidence geometry defined by the direction $\mathbf{Q}\|[hkl]$. Given $\mathbf{Q}\|[hkl]$, Eq. (44) reveals a maximum value of $\lambda_{\max}^{[hkl]}$ (the long-wavelength edge for a given direction) that is achieved depending on ϑ at a smallest allowed reflex index $(\mathbf{m})$. The largest value of $\lambda_{\max}^{[hkl]}$ over the all crystallographic directions is the absolute long-wavelength edge, above which light cannot diffract in the crystal.

For opals, in the $\mathbf{Q}\|[\bar{2}11]$ geometry Eq. (44) gives $\lambda_{\max}^{[\bar{2}11]}=a\sqrt{3\epsilon_0}$ for the $(\mathbf{m})=(0,\bar{1},0)$ reflex and the other reflexes related to the same circle in the 2D Ewald scheme in

Fig. 9(a). At $\mathbf{Q}\|[\bar{1}10]$, Eq. (44) and Fig. 9(b) provide $\lambda_{\max}^{[\bar{1}10]}=3a\sqrt{\epsilon_0}/2$, so $\lambda_{\max}^{[\bar{2}11]}/\lambda_{\max}^{[\bar{1}10]}=2\sqrt{3}/3>1$. The calculated values $\lambda_{\max}^{[\bar{2}11]}=650$ nm and $\lambda_{\max}^{[110]}=560$ nm satisfy the above expressions at $a\sqrt{\epsilon_0}\simeq 375$ nm. Turning again to the experimental patterns in Fig. 8, we conclude that the threshold quenching of monochromatic diffraction spots with the changing angle occurs when the related long-wavelength edge becomes shorter than the incident λ. At $\lambda=515$ nm, diffraction spots are actually observed for both the $\mathbf{Q}\|[\bar{2}11]$ and $\mathbf{Q}\|[\bar{1}10]$ incidence [Fig. 8(a)], in agreement with the condition $\lambda<\lambda_{\max}^{[\bar{1}10]}<\lambda_{\max}^{[\bar{2}11]}$, allowing both diffraction events. Figures 8(b) and 8(c) shows diffraction patterns for $\mathbf{Q}\|[\bar{2}11]$ at $\lambda=578$ nm and $\lambda=633$ nm with $\lambda_{\max}^{[\bar{1}10]}<\lambda<\lambda_{\max}^{[\bar{2}11]}$, and no spots are observed for $\mathbf{Q}\|[\bar{1}10]$. This is because both λ values exceed the long-wavelength edge for this direction and light is not diffracted by the sample.

In the (*i*) geometry, the long wavelength of the diffracted light, $\lambda_{\max}^{[\bar{1}\bar{1}\bar{1}]}=2a\sqrt{2\epsilon_0/3}$, is derived from Eq. (32) in the $\mathbf{Q}\|[\bar{1}\bar{1}\bar{1}]$ geometry at $\chi=\sqrt{3/2}$, $\vartheta=0$, $m_3=1$, corresponding to the (111) diffraction in the fcc lattice. The long-wavelength edge $\lambda_{\max}^{[\bar{1}\bar{1}\bar{1}]}=610$ nm measured at $\vartheta=0$ for our samples is in good agreement with the theoretical value. A comparison of the long-wavelength edges $\lambda_{\max}^{[\bar{1}\bar{1}\bar{1}]}<\lambda_{\max}^{[\bar{2}11]}$ measured in the (*i*) and (*ii*) geometries have shown that $\lambda_{\max}^{[\bar{2}11]}=650$ nm is the absolute long-wavelength edge for our samples. In the range $610<\lambda<650$ nm, the diffraction from a single layer or a few layers studied in this work was found to be unaffected by the other diffraction processes, including the commonly studied diffraction from the {111} planes.

Note that a pattern with *two* spots registered in the $[\bar{2}11]$ geometry at $\lambda<\lambda_{\max}^{[\bar{2}11]}$ transforms to a *one*-spot pattern at $\lambda=\lambda_{\max}^{[\bar{2}11]}$. A *four*-spot pattern registered in the $[\bar{1}10]$ geometry at $\lambda<\lambda_{\max}^{[\bar{1}10]}$ changes to a *two*-spot pattern at $\lambda=\lambda_{\max}^{[\bar{1}10]}$. This effect was observed in the $[\bar{1}10]$ geometry in monochromatic laser light with $\lambda=578$ nm, which is close to the calculated red diffraction edge $\lambda_{\max}^{[\bar{1}10]}\approx 560$ nm for this direction. The theory does not predict *four* spots at this wavelength, while the $[\bar{1}10]$ pattern seems to have two diffuse spots along the vertical axis [Fig. 8(b)].

E. Diffraction in the $\mathbf{Q}\|[\bar{1}10]$ geometry as a probe for sample quality

Next, we discuss the results of the diffraction experiments that allowed an estimation of the degree of structural disorder of opals and an identification of the best-ordered regions on the sample suitable for precise measurements. The most informative incidence geometry appeared to be that with $\mathbf{Q}\|[\bar{1}10]$. Figure 11 shows the diffraction patterns registered in this geometry on illumination with monochromatic light. It is found that some small regions on the sample produce only *two* spots each, as shown in Figs. 11(a) and 11(b). The

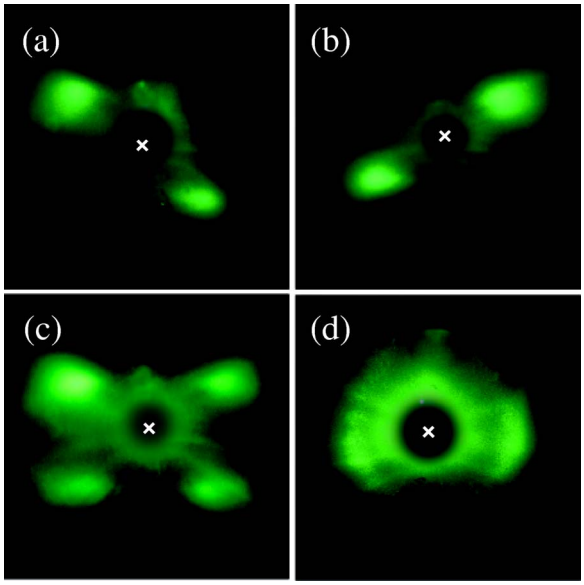

FIG. 11. (Color online) Diffraction patterns from various sample regions in the $\mathbf{Q}\|[\bar{1}10]$ incidence geometry at $\lambda=515$ nm: (a), (b) best-ordered monodomains of the fcc-I and fcc-II lattices; (c) a slightly disordered region of fcc twins; (d) a strongly disordered region made up of numerous microcrystallites with their growth axes oriented randomly relative to one another.

two pairs of spots are seen to be mirror symmetric relative to the [111] direction. Careful measurements showed that actually each diffraction pattern contained, in addition to a pair of intense spots, a pair of mirror symmetric spots of much lower intensity, such that they are visually undetectable in Figs. 11(a) and 11(b). The atomic-force microscopic and optical spectroscopic data demonstrated that the small areas producing this type of pattern possessed the most perfect structure.[15] However, the typical $\mathbf{Q}\|[\bar{1}10]$ patterns presented in Fig. 11(c) consisted of *four* visually observed spots.

We offer the following interpretation of the diffraction patters obtained in our experiments. Opals may possess two types of fcc structure representing sequences of …ABCABC… layers (fcc-I) and …CBACB… layers (fcc-II) illustrated in Fig. 2. In Bragg diffraction, a fcc-I structure would give the type of pattern shown in Fig. 11(a), while a fcc-II structure would produce a mirror symmetric pattern, like the one in Fig. 11(b). Therefore, the $\mathbf{Q}\|[\bar{1}10]$ diffraction from a perfect fcc lattice (a monodomain opal sample) cannot produce the pattern with four spots shown in Fig. 11(c). But this pattern can be obtained as a superposition of the patterns presented in Figs. 11(a) and 11(b). This indicates that the patterns in Fig. 11(c) are due to the coexistence of the fcc-I and fcc-II lattices alternating along the [111] growth axis. These adjacent domains having a common interface form a twinned fcc structure (such opal twins have been identified by electron microscopy[31]). If the beam width was larger than the characteristic size of the fcc-I and fcc-II domains, the diffraction from the twinned structure produced four spots, one pair of spots from the fcc-I and the other from the fcc-II structure. When the domain size was larger than the beam width, the diffraction pattern contained only one pair of spots

typical of a single fcc structure, Fig. 11(a) and 11(b).

Turn now to the discussion of diffraction from the most strongly disordered opal samples. The results of structural and optical studies show that (111) hcp layers can form not only a twinned fcc structure with embedded 3D hcp domains but also a structure made up of numerous microcrystallites with their growth axes oriented randomly relative to one another.[15] The microcrystallites may have both the fcc and hcp lattice, as well as the structure with 1D disorder of alternating closely packed layers. The diffraction pattern for a sample region with maximum disorder is illustrated in Fig. 11(d). It is similar to the Debye pattern but its diffracted light cone is in the backscattering geometry, and the diffraction is due only to one set of {111} planes. Bearing in mind the orientation of fcc domains mentioned previously, we can interpret this pattern in a way similar to that of x-ray diffraction patterns of powders: a mixture of numerous microcrystallites with a random orientation of the growth axes may always contain crystallites obeying the Bragg condition at a given wavelength λ.[1] Monochromatic light beams diffracted by such crystallites produce a cone with the angle Θ' at the vertex,[37] making a *circle* on a flat screen. Therefore, the diffraction spots from a strongly disordered opal sample degrade to form a *ring*.

We have shown that diffraction patterns obtained by illumination of synthetic opals with monochromatic light allow a visual evaluation of the degree of structural perfection of the sample under study. Thus, one can test the initial sample for regions with the best structure. For completeness, it should be noted that more opal-like and colloidal materials of various structure and perfection become technologically available.[13,44] In the same time, studied theoretically and experimentally are the optical spectra of disordered photonic crystals, influenced by polydispersity,[45] stacking faults,[32,46] the disorder-induced coherent multiple-scattering effects,[47] etc. All this means that for opal-like structures a field exists for extending the above ideas on the Bragg diffraction.

VI. CONCLUSION

Our experimental and theoretical study of the Bragg diffraction of light in synthetic opals has shown that opal-based photonic crystals manifested itself as 3D diffraction gratings to *visible light*. By special choosing of the a-SiO_2 spheres sizes, we have visualized the principal Bragg diffraction features such as angle and wavelength dependencies of 3D diffraction patterns, the existence of a long-wavelength edge, the interlayer and orientation disorder effects in diffraction patterns. It is demonstrated that the scattering of monochromatic light by the crystal lattice of high quality opals appears on the screen as symmetric sets of diffraction spots. The presence of the bright spots due to the Bragg reflection of visible light by the {111} planes of a twinned fcc structure is specific of the diffraction patterns. We also analyzed the evolution of the patterns from a highly ordered samples to ones with a twinned fcc lattice and further to a strongly disordered samples made up of disoriented microcrystallites. A light diffraction theory is developed for opal-like structures with a random alternation of the closely packed growth layers. Within this theory, we have offered an interpretation of the observed spectral angular characteristics and found the long-wavelength diffraction edge and its variation with the light incidence relative to the fcc lattice.

An essential structural feature of ordered opals is that the hcp growth layers of closely packed silica spheres possess a long-range 2D ordering at macroscopic distances. The 1D interlayer disorder along the growth axis allowed the observation of a very informative and diverse diffraction patterns possessing characteristics typical of both 2D and 3D structures. This type of pattern is interpreted in terms of the suggested theory and is shown to be consistent with the characteristic size of random domains in the fcc lattice of an opal twin structure.

ACKNOWLEDGMENTS

We thank A. A. Kaplyanskii for numerous helpful discussions and support, M. I. Samoilovich for the preparation of the samples, and A. V. Ankudinov, M. V. Rybin, and A. K. Samusev for experimental assistance. This work was supported in parts by the Russian Foundation for Basic Research (Grants No. 05-02-17809 and No. 04-02-17592).

APPENDIX:

We use the following unit translations:

$$\hat{\mathbf{a}}_1 = \frac{a}{2}(-\hat{\mathbf{x}}\sqrt{3} + \hat{\mathbf{z}}), \quad \hat{\mathbf{a}}_2 = \frac{a}{2}(\hat{\mathbf{x}}\sqrt{3} + \hat{\mathbf{z}}),$$
$$\hat{\mathbf{a}}_3 = \frac{a}{2}\left(\frac{1}{\sqrt{3}}\hat{\mathbf{x}} + \frac{2}{\chi}\hat{\mathbf{y}} + \hat{\mathbf{z}}\right), \tag{A1}$$

expressed in the "in-crystal" coordinate system shown in Fig. 1(b). The vectors $\hat{\mathbf{a}}_1$ and $\hat{\mathbf{a}}_2$ define the lattice of a single hcp layer with the intersite distance a. In general, since the vector $\hat{\mathbf{a}}_3$ depends on the interlayer spacing A through the parameter $\chi = a/A$, it refers to a single hcp layer at $\chi \to 0$ and to a fcc lattice at $\chi = \chi_{\max} = \sqrt{3/2}$. Equations (A1) yields the following reciprocal lattice vectors:

$$\hat{\mathbf{b}}_1 = \frac{2\pi}{a}\left(-\hat{\mathbf{x}}\frac{1}{\sqrt{3}} + \hat{\mathbf{z}} - \frac{1}{3}\chi\hat{\mathbf{y}}\right),$$
$$\hat{\mathbf{b}}_2 = \frac{2\pi}{a}\left(\hat{\mathbf{x}}\frac{1}{\sqrt{3}} + \hat{\mathbf{z}} - \frac{2}{3}\chi\hat{\mathbf{y}}\right), \quad \hat{\mathbf{b}}_3 = \frac{2\pi}{a}\chi\hat{\mathbf{y}}. \tag{A2}$$

In the limit $\chi \to 0$ of a single hcp layer, the vectors (A2) become

$$\hat{\mathbf{b}}_1^0 = \frac{2\pi}{a}\left(-\hat{\mathbf{x}}\frac{1}{\sqrt{3}} + \hat{\mathbf{z}}\right), \quad \hat{\mathbf{b}}_2^0 = \frac{2\pi}{a}\left(\hat{\mathbf{x}}\frac{1}{\sqrt{3}} + \hat{\mathbf{z}}\right), \quad \hat{\mathbf{b}}_3^0 = 0. \tag{A3}$$

In analyzing Eq. (24), the vectors entering both Eqs. (A1) and (A2) are expressed through the unit vectors $\hat{\mathbf{e}}_\alpha$ using the Euler angles. Given the indices m_i in Eq. (24) for the reference fcc-I lattice with (A2) and $\chi = \sqrt{3}/2$, the Miller indices (hkl) defined in the reference coordinate system, whose unit vectors are parallel to [100], [010], and [001], are

$$h{:}k{:}l = (-m_1 - 2m_2 + m_3){:}(m_1 + m_3){:}(-m_1 + m_3). \tag{A4}$$

When treating the diffraction for the complementary (fcc-II) lattice, one should take all the vectors (A1)–(A3) with the opposite signs.[36]

[1] Ch. Kittel, *Introduction to Solid State Physics*, 6th ed. (Wiley, New York, 1986).

[2] J. C. Slater, *Insulators, Semiconductors and Metals. Quantum Theory of Molecules and Solids* (McGraw-Hill, New York, 1967), Vol. 3.

[3] J. D. Joannopoulos, R. D. Meade, and J. N. Winn, *Photonic Crystals: Molding the Flow of Light* (Princeton University Press, Princeton, NJ, 1995).

[4] E. Yablonovitch, Phys. Rev. Lett. **58**, 2059 (1987); E. Yablonovitch and T. J. Gmitter, *ibid.* **63**, 1950 (1989).

[5] *Photonic Band Gap Materials*, edited by C. M. Soukoulis, NATO ASI Series E, 1996, Vol 315, 1996.

[6] V. N. Astratov, V. N. Bogomolov, A. A. Kaplyanskii, A. V. Prokofiev, L. A. Samoilovich, S. M. Samoilovich, and Yu. A. Vlasov, Nuovo Cimento D **17**, 1349 (1995).

[7] V. N. Astratov, Yu. A. Vlasov, O. Z. Karimov, A. A. Kaplyanskii, Yu. G. Musikhin, N. A. Bert, V. N. Bogomolov, and A. V. Prokofiev, Phys. Lett. A **222**, 349 (1996).

[8] Yu. A. Vlasov, V. N. Astratov, O. Z. Karimov, A. A. Kaplyanskii, V. N. Bogomolov, and A. V. Prokofiev, Phys. Rev. B **55**, R13357 (1997).

[9] V. N. Bogomolov, S. V. Gaponenko, I. N. Germanenko, A. M. Kapitonov, E. P. Petrov, N. V. Gaponenko, A. V. Prokofiev, A. N. Ponyavina, N. I. Silvanovich, and S. M. Samoilovich, Phys. Rev. E **55**, 7619 (1997).

[10] A. Reynolds, F. Lopez-Tejeira, D. Cassagne, F. J. Garcia-Vidal, C. Jouanin, and J. Sanchez-Dehesa, Phys. Rev. B **60**, 11422 (1999).

[11] H. Miguez, A. Blanco, F. Meseguer, C. Lopez, H. M. Yates, M. E. Pemble, V. Fornes, and A. Mifsud, Phys. Rev. B **59**, 1563 (1999).

[12] Yu. A. Vlasov, V. N. Astratov, A. V. Baryshev, A. A. Kaplyanskii, O. Z. Karimov, and M. F. Limonov, Phys. Rev. E **61**, 5784 (2000).

[13] Yu. A. Vlasov, X.-Z. Bo, J. C. Sturm, and D. J. Norris, Nature **414**, 289 (2001).

[14] V. N. Astratov, A. M. Adawi, S. Fricker, M. S. Skolnick, D. M. Whittaker, and P. N. Pusey, Phys. Rev. B **66**, 165215 (2002).

[15] A. V. Baryshev, A. V. Ankudinov, A. A. Kaplyanskii, V. A. Kosobukin, M. F. Limonov, K. B. Samusev, and D. E. Usvyat, Fiz. Tverd. Tela (S.-Petersburg) **44**, 1573 (2002) [Phys. Solid State **44**, 1648 (2002)].

[16] A. A. Zakhidov, R. H. Baughman, Z. Iqbal, C. Cui, I. Khairulin, S. O. Dantas, J. Marti, and V. G. Ralchenko, Science **282**, 897 (1998).

[17] V. G. Golubev, J. L. Hutchison, V. A. Kosobukin, D. A. Kurdyukov, A. V. Medvedev, A. B. Pevtsov, J. Sloan, and L. M. Sorokin, J. Non-Cryst. Solids **299-302**, 1062 (2002).

[18] V. G. Golubev, V. A. Kosobukin, D. A. Kurdykov, A. V. Medvedev, and A. B. Pevtsov, Fiz. Tekh. Poluprov. (S.-Petersburg) **35**, 710 (2001) [Semiconductors **35**, 680 (2001)].

[19] J. E. G. J. Wijnhoven and W. L. Vos, Science **281**, 802 (1998).

[20] M. S. Thijssen, R. Sprik, J. E. G. J. Wijnhoven, M. Megens, T. Narayanan, A. Lagendijk, and W. L. Vos, Phys. Rev. Lett. **83**, 2730 (1999).

[21] H. M. van Driel and W. L. Vos, Phys. Rev. B **62**, 9872 (2000).

[22] I. I. Tarhan and G. H. Watson, Phys. Rev. Lett. **76**, 315 (1996); V. Yannopapas, N. Stefanou, and A. Modinos, J. Phys.: Condens. Matter **9**, 10261 (1997).

[23] R. M. Amos, J. G. Rarity, P. R. Tapster, T. J. Shepherd, and S. C. Kitson, Phys. Rev. E **61**, 2929 (2000).

[24] S. G. Romanov, T. Maka, C. M. Sotomayor Torres, M. Müller, R. Zentel, D. Cassagne, J. Manzanares-Martinez, and C. Jouanin, Phys. Rev. E **63**, 056603 (2001).

[25] J. F. Galisteo-Lopez, E. Palacios-Lidon, E. Castillo-Martinez, and C. Lopez, Phys. Rev. B **68**, 115109 (2003).

[26] A. V. Baryshev, A. A. Kaplyanskii, V. A. Kosobukin, K. B. Samusev, D. E. Usvyat, and M. F. Limonov, Phys. Rev. B **70**, 113104 (2004).

[27] J. V. Sanders, Acta Crystallogr., Sect. A: Cryst. Phys., Diffr., Theor. Gen. Crystallogr. **24**, 427 (1968).

[28] S. A. Asher, J. M. Weissman, A. Tikhonov, R. D. Coalson, and R. Kesavamoorthy, Phys. Rev. E **69**, 066619 (2004).

[29] F. García-Santamaría, J. F. Galisteo-López, P. V. Braun, and C. López, Phys. Rev. B **71**, 195112 (2005).

[30] A. Guinier, *X-Ray Diffraction* (Freeman, San Francisco, 1963).

[31] L. M. Sorokin, V. N. Bogomolov, J. L. Hutchison, D. A. Kurdyukov, A. V. Chernyaev, and T. N. Zaslavskaya, Nanostruct. Mater. **12**, 1081 (1999).

[32] V. Yannopapas, N. Stefanou, and A. Modinos, Phys. Rev. Lett. **86**, 4811 (2001).

[33] J. M. Ziman, *Models of Disorder. The Theoretical Physics of Homogeneously Disordered Systems* (Cambridge University Press, Cambridge, 1979).

[34] H. Jeffreys and B. Swirles, *Methods of Mathematical Physics* 3rd ed. (Cambridge University Press, Cambridge, 1966).

[35] V. A. Kosobukin, Surf. Sci. **406**, 32 (1998).

[36] To describe the kinematics of diffraction in this paper, the following coordinate systems are used (Fig. 1): (a) the system with the unit vectors $\mathbf{e}_\alpha$ to define the wave vectors (7) and (12); (b) the crystallographic system with the unit vectors $\hat{\mathbf{X}} \| [100]$, $\hat{\mathbf{Y}} \| [010]$, and $\hat{\mathbf{Z}} \| [001]$, in which the Miller indices of the fcc-I lattice is

defined; (c) the coordinate system with the unit vectors $\hat{\mathbf{x}}$, $\hat{\mathbf{y}}$, and $\hat{\mathbf{z}}$, in which the diffraction effects of a single hcp layer and a layer stack are separated, in accordance with Eq. (20). The Miller indices for the direction of the wave vector $\mathbf{Q}$ in the crystal and the set of diffracting (hkl) planes are determined with respect to the reference (fcc-I) lattice, with the symbol (hkl) expressed by the formula (A4) through the indices (m_1, m_2, m_3) entering Laue's equations (24). Equations (24) or (26) for the fcc-II lattice can be conveniently treated in the coordinate system, whose unit vectors are obtained by the inversion of $\hat{\mathbf{x}}$, $\hat{\mathbf{y}}$, and $\hat{\mathbf{z}}$. For an incident wave with a given vector $\mathbf{Q}$, the indices (m_1, m_2, m_3) and (hkl) of the planes responsible for the diffraction from the fcc-I and fcc-II lattices will differ in the sign.

[37] The experimental registration angle $-90° < \Theta' < 90°$ for the $\mathbf{Q} \| (111)$ incidence is defined in terms of the angles ϑ' and φ' as $\Theta' = -\vartheta' < 0$ at $\cos\varphi' < 0$ and as $0 < \Theta' = \vartheta'$ at $\cos\varphi' > 0$.

[38] W. Loose and B. J. Ackerson, J. Chem. Phys. **101**, 7211 (1994).

[39] A. V. Baryshev, A. A. Kaplyanskii, V. A. Kosobukin, M. F. Limonov, and A. P. Skvortsov, Phys. Solid State **46**, 1331 (2004).

[40] N. Stefanou, V. Yannopapas, and A. Modinos, Comput. Phys. Commun. **113**, 49 (1998); **132**, 189 (2000).

[41] K. Busch and S. John, Phys. Rev. E **58**, 3896 (1998).

[42] A. Moroz, Phys. Rev. B **51**, 2068 (1995); A. Moroz and C. Sommers, J. Phys.: Condens. Matter **11**, 997 (1999).

[43] A. V. Baryshev, A. A. Kaplyanskii, V. A. Kosobukin, M. F. Limonov, K. B. Samusev, and D. E. Usvyat, Fiz. Tverd. Tela (S.-Petersburg) **45**, 434 (2003) [Phys. Solid State **45**, 459 (2003)].

[44] J. P. Hoogenboom, D. Derks, P. Vergeer, and A. van Blaaderen, J. Chem. Phys. **117**, 11320 (2002); J. P. Hoogenboom, A. K. van Langen-Suurling, H. Romijn, and A. van Blaaderen, Phys. Rev. Lett. **90**, 138301 (2003).

[45] R. Rengarajan, D. Mittleman, C. Rich, and V. Colvin, Phys. Rev. E **71**, 016615 (2005).

[46] Z. L. Wang, C. T. Chan, W. Y. Zhang, Z. Chen, N. B. Ming, and P. Sheng, Phys. Rev. E **67**, 016612 (2003).

[47] V. Yannopapas, A. Modinos, and N. Stefanou, Phys. Rev. B **68**, 193205 (2003).